Strength prediction in NiCo alloys — The role of composition and nanotwins

P. Chowdhury [a], H. Sehitoglu [a, *], H.J. Maier [b], R. Rateick [c]

[a] Department of Mechanical Science and Engineering, University of Illinois at Urbana-Champaign, 1206 W. Green St., Urbana, IL 61801, USA
[b] Institut für Werkstoffkunde (Materials Science), Leibniz Universität Hannover, D-30823 Garbsen, Germany
[c] Honeywell Aerospace, 3520 Westmoor St., South Bend, IN 46628, USA

ARTICLE INFO

ABSTRACT

Experimentally, hardening behaviors of nano-twinned Ni—Co alloys in tension demonstrate strong composition dependence. The strengthening characteristics improve substantially with increasing Co content (up to 2.9% Co), however, accompanied by an abrupt decline (at 5.52% Co), suggesting the existence of a critical composition. On theoretical grounds, atomistic modeling is performed to rationalize the experimental observations. First, the origin of Co content effects is traced back to an atomic level competition between solid solution hardening and Suzuki segregation processes, resulting in a non-uniform γ surface variation. Secondly, the different slip transfer mechanisms across a coherent twin boundary are found to experience altered degrees of unstable fault energies (γ_{us}) owing to various residual dislocations. With evolving incident/residual slip, the γ_{us} values first increase, and then attain saturated levels. Thus-computed γ_{us} magnitudes are converted into corresponding frictional stresses within a Peierls-Nabarro modeling framework. Then, critical resolved shear stresses (CRSS) are predicted for different Ni—Co alloys. In conclusion, the apparently puzzling trends in the Ni—Co macroscopic strengths can be both qualitatively and quantitatively theorized by considering the combined effects of: (a) the twin influenced slip activities at the mesoscale and (b) the alloying induced fault energetics at the quantum scale.

© 2015 Elsevier Ltd. All rights reserved.

1. Introduction

The microstructure-property correlation in metals and alloys has remained an important topic of research endeavors throughout the last century. Significant progresses were made in the 1950s through the early 1980s establishing important phenomenological laws (Bailey and Hirsch, 1960; Basinski and Basinski, 1964; Estrin and Mecking, 1984; Rice, 1971; Seeger et al., 1957). With the advent of major innovations in materials processing and testing, the last decade in particular has witnessed considerable developments in the knowledge of microplasticity that shape our modern understanding of microstructural influences on deformation response (Chaboche et al., 2013; Gleiter, 2000; McDowell, 2010; Meyers et al., 2006; Valiev, 2004; Witkin and Lavernia, 2006). For the current generation of scientists and researchers, advancement of novel alloys essentially requires delving deeper into an atomic level understanding of the structure—property relationship

---

* Corresponding author. Tel.: +1 217 333 4112; fax: +1 217 244 6534.
E-mail address: huseyin@illinois.edu (H. Sehitoglu).

devoid of empiricism. Given the vast improvements in computational materials science tools (Cheng and Ngan, 2013; Dreizler and Engel, 2011; Tadmor and Miller, 2011), we deem it timely and necessary to make major strides in establishing material laws informed by underlying atomic physics, free of empirical constants from a new perspective. To that end, we build on the foundation laid by the most contemporary knowledge of microplasticity at various lengthscales of relevant operative flow mechanisms (Abuzaid et al., 2012; Asaro and Suresh, 2005; Austin and McDowell, 2011; Cai et al., 2004; Collins and Stone, 2014; Deng and Sansoz, 2009b; Li and Ghoniem, 2009; Lu et al., 2009b; Tadmor and Miller, 2011). The current research emphasizes on a synergistic modeling approach, which bridges atomistic and mesoscale theories with experimental hardening behavior, considering a case study of electrodeposited nano-twinned Ni–Co alloys of different compositions. The consideration of nano-twinned alloy as the candidate material for this study is rooted upon the recently growing research interests therein (Lu et al., 2009a; Zhu et al., 2015; Zhu et al., 2011a) due to the prospect of drastic improvement of mechanical properties. The current undertaking begins with the documentation of experimental stress-strain responses of electro-deposited nano-structured NiCo alloys along with extensive analyses on pre- and post-deformation microstructures. On modeling grounds, firstly we isolate the effects of alloy composition in terms of material fault energetics from first principles. Subsequently, the role of coherent twin boundaries on mesoscale slip characteristics has been extensively investigated using molecular dynamics simulations. A unified theory combining atomic level solute effects and mesoscale strain transfer mechanisms is offered to rationalize the continuum hardening behaviors as observed experimentally.

Early literature notes that the significant improvement in polycrystalline strengthening attributes can be accomplished via grain refinement strategies (Gu and Ngan, 2013; Kumar et al., 2003). The correlation between the grain size and the hardening behavior is described phenomenologically by the classical Hall-Petch type formulations (Hall, 1951; Petch, 1953). The genesis of the Hall-Petch effects has been ascribed to an amplified degree of dislocation slip obstruction (Asaro and Suresh, 2005; Baker, 2001; Narutani and Takamura, 1991) as a consequence of an increased volume fraction of slip-obstacles (i.e. grain boundaries). However, improved strength due to reduced grain size in conventional coarse-grained materials occurs at the significant expense of ductility. On the other hand, metallic microstructure rife with thermally stable nano-sized annealing twins reportedly demonstrate high strengthening attributes with the retention of substantial ductility (Lu et al., 2004). Recent literature suggested that widespread distribution of annealing twins serves to divide the host grains into multiple sub-grain type segments (Fig. 1). As a result, the sheer presence of additional interfacial obstacles (i.e. the coherent twin boundaries) contributes to the macroscopic strength, to the same effect as the grain refinement (Li et al., 2010). However, the preceding argument does not hold when it comes to explaining the retention of relatively high ductility upon introducing nano-sized twins in the microstructure. In order to elucidate the beneficial attributes of nano-twinned microstructure, a number of theoretical studies ventured into the mechanistic origin of combined high strength and ductility on the basis of various slip twin boundary interaction mechanisms (Asaro and Kulkarni, 2008; Deng and Sansoz, 2009a; Hartley and Blachon, 1978; Kacher et al., 2014; Mahajan and Chin, 1973; Wu et al., 2009; Zhu and Gao, 2012; Zhu et al., 2011b). It has been suggested that a coherent twin boundary can uniquely provide complete or partial or no transfer of the impinging slip, depending on the
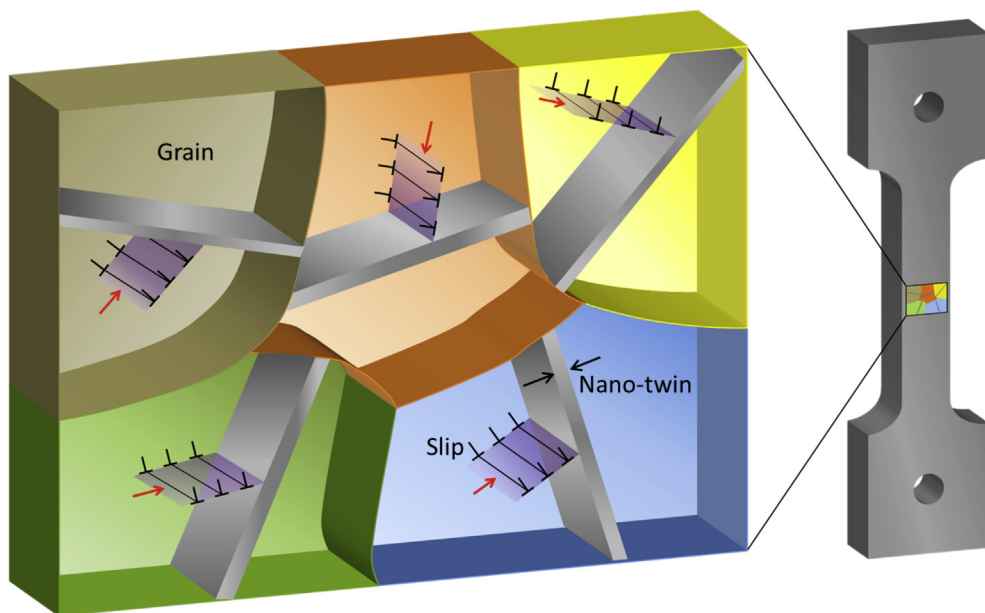

Fig. 1. Annealing nano-twins obstructing slip. Differently oriented grains have different local stress states triggering various slip transfer mechanisms across the twin boundaries.

local stress situation and geometric considerations. Moreover, unlike most commonly encountered grain interface types, a pristine twin boundary can allow for significant degree of glissile motion on the interface, leading to a twin migration process to which the origin of superior ductility has been attributed by some researchers (Zhu et al., 2007). In the earlier literature, the conditions for the outcome of slip intercepting a generic grain boundary has been experimentally established (Lee et al., 1990) as follows − (a) maximization of local resolved shear stress, (b) minimization of angle between incoming and outgoing slip plane and (c) minimization of residual Burgers vector. The slip transfer mechanisms are also expected to vary from grain to grain abiding by the foregoing rules, due to differences in grain orientations (Fig. 1).

From a non-continuum perspective, widespread introduction of nano-sized annealing twins in the material microstructure would be manifested as a considerable variation in the overall Peierls energy barrier landscape. In a nano-twinned material, owing to an abundance of the coherent twin boundaries, the average Peierls energy barrier for each grain would be considerably greater than that of conventional coarse-grained counterparts. As a result, a higher magnitude of external forces would be required to sustain adequate dislocation activities during plastic deformation. Intuitively, the magnitude of critical resolved shear stress, τ_{CRSS}, in the presence of an increased number of slip-barriers would be considerably augmented. In the Peierls-Nabarro formalisms, the theoretical value of τ_{CRSS} is a direct function of the so-called unstable stacking fault energy, γ_{us} (Hirth and Lothe, 1982; Lu, 2005; Nabarro, 1947; Peierls, 1940). The γ_{us} is defined as the maximum value on the energy−displacement curve during rigid shear of two crystal blocks, known as the generalized stacking fault energy (GSFE) or γ surface (Rice, 1992; Vitek, 1968). The intrinsic magnitude of the γ_{us} represents the energy barrier for free dislocation glide. Conventionally, the γ_{us} can only be determined from first principles or molecular statics energy minimization procedure. Moreover, the extrinsic levels of the γ_{us} for glide under the influence of a residual dislocation, $\vec{b}_r = \vec{b}_{incoming} - \vec{b}_{transferred}$, can be computed using molecular dynamics simulations during the actual motion of a dislocation (Chowdhury et al., 2013; Ezaz et al., 2011; Sangid et al., 2012). The $\vec{b}_r$ is created upon the twin boundary when an incoming dislocation from the matrix material, $\vec{b}_{incoming}$, intercepts the interface, and transfers slip inside the twin, $\vec{b}_{transferred}$. Utilizing the foregoing concepts, we propose a comprehensive theory to answer the long-standing question of microstructure-property correlation in nano-twinned binary Ni−Co alloys.

We conduct uniaxial tension experiments on Ni−Co alloys, and the critical resolved shear stresses are determined. Ex-situ electron backscatter diffraction (EBSD) scans establish the grain orientation map, giving insight into the surface texture. Transmission electron microscopy (TEM) is used to reveal the prevalence of nano-scale annealing twins, and the widespread twin boundary-slip interception during plastic deformation. Extensive molecular dynamics simulations are conducted to investigate various slip-twin boundary interaction mechanisms, and the associated evolution of the energy parameter, γ_{us}. Using density functional theory (DFT) simulations, we capture the alloying-induced γ surface. Combining quantum calculations and the molecular dynamics simulations, the critical resolved shear stresses are predicted within the Peierls-Nabarro modeling framework. The proposed theory is used to rationalize the experimentally observed deformation behavior of the nano-structured Ni−Co alloys in question. The current approach is schematically summarized in Fig. 2.

2. Methods

2.1. Material preparation and tension experiment

The Ni−Co alloys (of 1%, 1.62%, 2.9% and 5.52% Co by weight) were fabricated with an electrodeposition process by NiCoForm Inc. Tension experiments were conducted at room temperature. The textures of the Ni−Co alloys were studied using high resolution electron back-scatter diffraction (EBSD). Transmission electron microscopy (TEM) was used to study the microstructure at the nanometer scale. More information regarding the sample preparation and test procedure can be found in (Sangid et al., 2011).

2.2. Density functional theory (DFT)

For DFT calculations, we used the Vienna ab initio simulation package (VASP) (Kresse and Furthmüller, 1996). The crystal configurations were studied using Visual Molecular Dynamics (http://www.ks.uiuc.edu/Research/vmd/) (Humphrey et al., 1996). Solid solutions of various compositions of Ni−Co alloys were energetically minimized iteratively. A more detailed description of the DFT method used in the current work can be found in (Chowdhury et al., 2015). Critical discussions particularly relevant to the current work are also provided in Appendix A.

2.3. Molecular dynamics (MD)

For the MD simulations, the open-source software LAMMPS (Large-scale Atomic/Molecular Massively Parallel Simulator) developed at Sandia National Laboratories, USA (http://lammps.sandia.gov) (Plimpton, 1995) was used. The atomic configuration viewer AtomEye (Li, 2003) (http://li.mit.edu/Archive/Graphics/A/), was used to calculate the fault energy profile during the glide of a dislocation. Embedded atomic method (EAM) potentials from the literature by (Zhou et al., 2004) and (Pun and Mishin, 2012) (http://www.ctcms.nist.gov/potentials/Ni.html) were used to compare fault energetics with DFT data for Ni−Co alloys. Subsequently, for the slip-twin interactions study, the potential by Zhou et al. was used for comprehensive
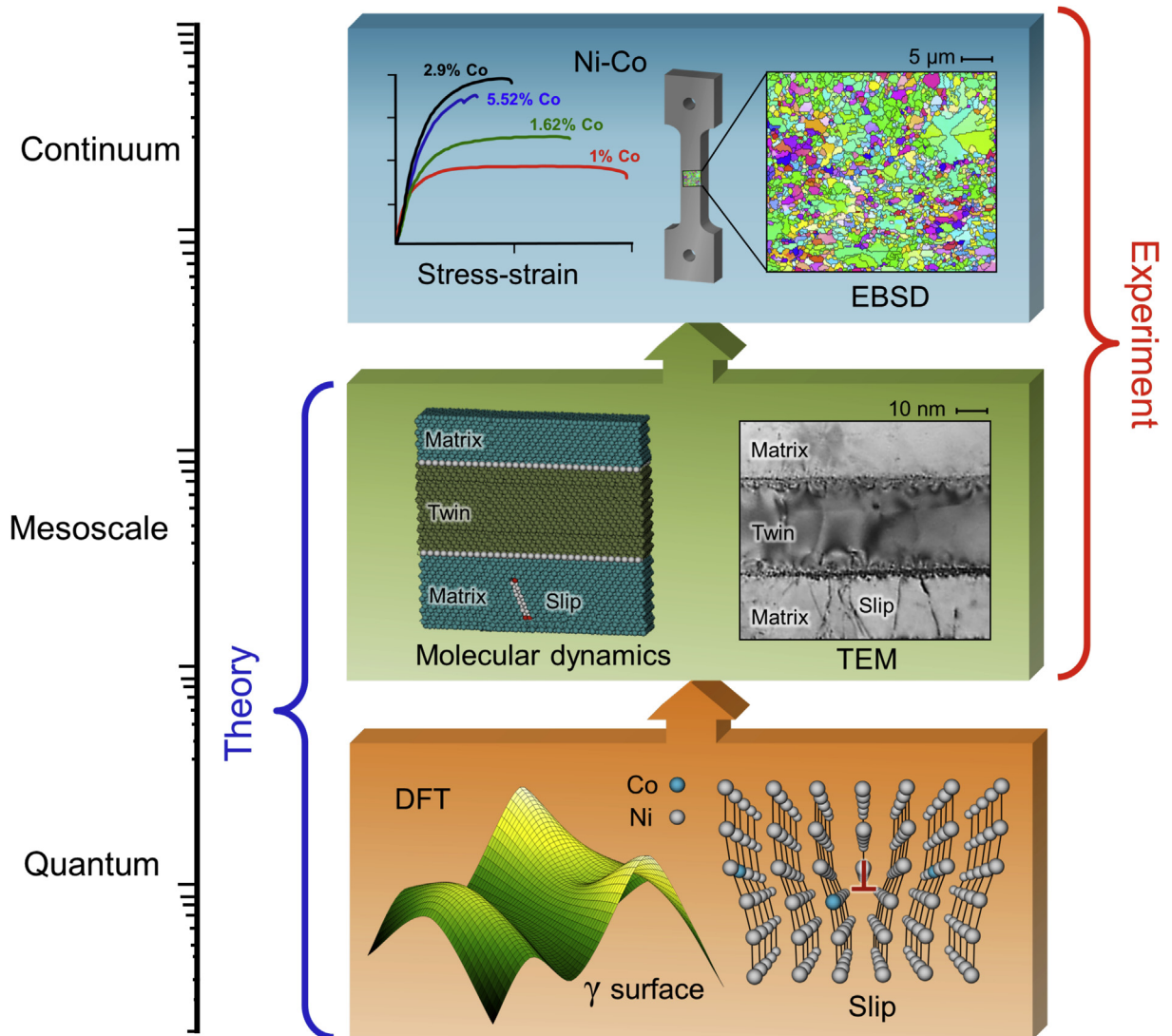
Fig. 2. The overall structure and scope of the current bottom-up approach spanning continuum, mesoscale and quantum lengthscale considerations.

molecular dynamics simulations of Ni–2.9% Co alloys (as a representative material). For further details of the MD procedure adopted in the current work, the readers are referred to (Chowdhury, 2011; Chowdhury et al., 2014a, 2013).

3. Experimental results — stress-strain response and microstructure

Fig. 3 demonstrates the stress–strain responses for the electrodeposited Ni–Co alloys. All these materials possess similar elastic slopes i.e. Young's moduli. However, their plastic hardening characteristics differ to a considerable extent from alloy to alloy. The alloy with 1% Co content has the lowest 0.2% offset yield strength (522 MPa) and hardening rate with the maximum extent of ductility (5.6% elongation). The Ni-1.62% Co alloy with a yield strength of 631 MPa has a reduced degree of elongation (4.2%). Further strength enhancement is demonstrated for the Ni-2.9% Co material, with pre-rupture elongation of 1.9%. Most interestingly, addition of Co beyond 2.9% results in an apparently opposing trend. Using a Taylor factor of 3.06, critical resolved shear stresses for the alloys are. A summary of tension experiment results is presented in Table 1.

The EBSD scans in Fig. 4(a) and (b) indicates that the Ni-1% Co alloy has a mild [011] texture. However, the Taylor factor is determined to be 3.06, a value indicative of a wide range of grain distribution (Sangid et al., 2011). Similar grain distribution is observed for other Ni–Co alloys (not shown) from EBSD.

Fig. 5(a)–(g) show the nano-twinned microstructure of Ni–Co alloys. The deformed material demonstrates a considerable degree of slip obstruction at the twin boundaries Quite interestingly, although the alloys have very similar microstructure, their macroscopic mechanical response differs significantly. In order to rationalize the foregoing experimental findings, atomistic modeling is performed.
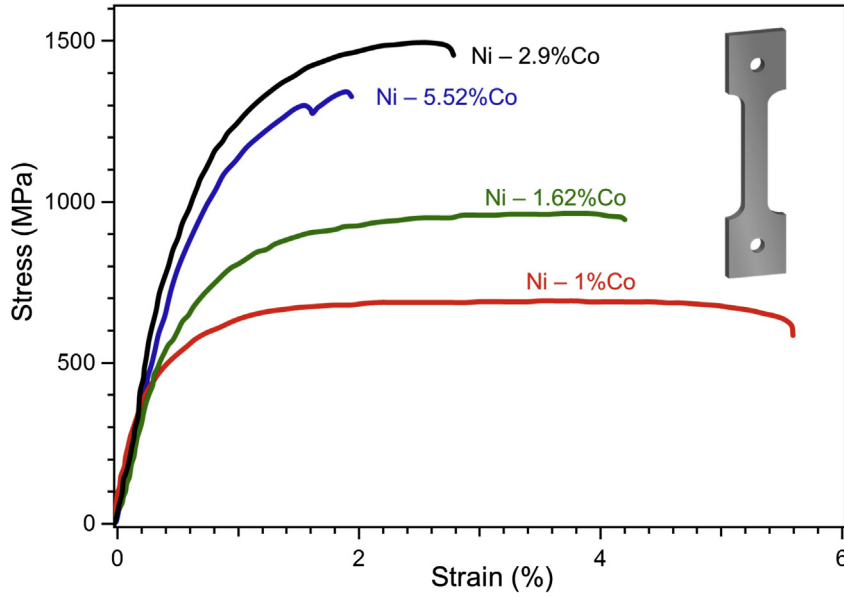
Fig. 3. Stress-strain response of the electrodeposited Ni−Co alloys − Ni−1.0% Co, Ni−1.62% Co, Ni-2.9% Co, and Ni−5.52% Co (Sangid et al., 2011).

4. Theoretical results

4.1. Ni−Co γ surface from first principles

Fig. 6 shows the γ surface for the Ni-2.9% alloy calculated via density functional theory (using the method described in Appendix A). The unstable stacking fault energy γ_{us} for $\langle 110 \rangle$ and $\langle 112 \rangle$ slip directions are found to be 360 mJ/m^2 and 305 mJ/m^2 respectively, and the intrinsic stacking fault energy γ_{isf} to be 153 mJ/m^2. The peak energy to further shear the crystal along the same $\langle 112 \rangle$ direction is very high (about 720 mJ/m^2). This indicates that the slip would occur predominantly along the $\langle 112 \rangle$ family of directions (i.e. forming partial dislocations separated by stacking fault plane). The parameters γ_{isf} and γ_{us} for Ni-1% Co, Ni-1.62% Co, Ni-2.9% Co and Ni-5.52% Co are provided Table 2. In Fig. 7(a), the current γ_{isf} data are compared with literature DFT (Chandran and Sondhi, 2011) and experimental values (Gallagher, 1970) as well as those computed using EAM potentials.

Fig. 7(a) shows that there exists a non-uniform γ_{isf} variation for <10% Co concentration. With increasing Co content, the γ_{isf} initially rises to a maximum value of 153 mJ/m^2 and then continues to drop. The same trend is also observed for γ_{us} values which are provided in Table 3. The rise portion is found to be caused by solid solution effects (i.e. the solute atoms providing additional resistance to the rigid shearing of the two blocks). By contrast, the gradually increasing presence of Co solutes triggers a solute segregation process in the vicinity of the fault. These two competing mechanisms give rise to the apparent the γ_{isf} non-uniformity for low Co concentration. This phenomenon is schematically illustrated in Fig. 7(b).

In the next step, we perform MD simulations to establish various slip transfer mechanisms in Ni-2.9% Co as the representative alloy.

4.2. Molecular dynamics slip-twin boundary interactions

Fig. 8(a) shows a single grain with an annealing twin constructed for conducting molecular dynamics (MD) simulations using Ni-2.9% Co as the representative Ni−Co alloy. A dislocation source (a void) is placed in the vicinity of the nano-twin in the matrix so as to facilitate nucleation and subsequent incidence of dislocation on the neighboring coherent twin boundary. The dislocation geometries are observed to be of extended type (i.e. a pair of leading and trailing Shockley partials of type a/6$\langle 112 \rangle$ connected by a plane of the stacking fault). Depending on the orientation of the single grain, various degrees of Schmid factor would be operative on the leading/trailing partials as in Fig. 8(b).

When a far-field load, σ_{ij} is applied on the twinned grain, dislocations nucleate in accordance with the Schmid law on the {111} family of planes. For the activated slip systems, the resolved shear stress, τ_{RSS} under the farfield applied stress, σ_{ij} is calculated, using Equation (1).

$$\tau_{RSS} = \sigma_{ij} n_i s_j \tag{1}$$

In Equation (1), σ_{ij} is the farfield stress tensor, n_i the slip plane normal vector, and s_i the vector representing the slip direction. The Schmid factor, m is defined as the ratio between the resolved shear stress, τ_{RSS} and the Tresca stress, σ_{Tresca} (i.e. maximum differential between the principal stresses) given in Equation (2). For example, τ_{xy} type pure shear applied loading leads to, $\sigma_{Tresca} = 2\tau_{xy}$, and for σ_{yy} type pure uniaxial tension, $\sigma_{Tresca} = \sigma_{yy}$.

Table 1
Experimentally determined mechanical properties of the current Ni–Co alloys.

	Young's Modulus, E (GPa)	Yield strength (0.2% offset), σ_y (MPa)	Critical resolved shear stress, $\tau_{CRSS} = \dfrac{\sigma_y}{3.06}$ (MPa)	Ultimate strength, σ_{UTS} (MPa)	Elongation (%) (until rupture)
Ni–1% Co	180	522	170.6	689	5.6
Ni-1.62% Co	159	631	206.2	961	4.2
Ni-2.9% Co	163	1304	426.2	1487	2.6
Ni-5.52% Co	165	1020	333.3	1332	1.9

$$m = \frac{\tau_{RSS}}{\sigma_{Tresca}} \qquad (2)$$

We observe that different reactions occur depending on various combinations of the Schmid factors on the incident, twin boundary and the outgoing slip systems (Table 3). In the next sections, we describe the reactions case-by-case with atomic configurations and a double Thompson tetrahedron representing the matrix and twin.

(a) Incorporation

On intercepting the twin boundary, the leading partial a/6[$\bar{2}1\bar{1}$] creates a twinning dislocation a/6[$\bar{1}2\bar{1}$] and a sessile stair rod dislocation. The trailing Shockley partial a/6[$\bar{1}21$] interacts with the sessile stair rod dislocation, and creates another twinning partial a/6[$\bar{2}11$]. The overall reaction is summarized by Equation (3) and by the double tetrahedron in Fig. 9(a).

$$\underbrace{\frac{a}{6}[\bar{2}1\bar{1}] \;+\; \frac{a}{6}[\bar{1}21]}_{\text{Incident (Matrix)}} \;\rightarrow\; \underbrace{\frac{a}{6}[\bar{1}2\bar{1}] \;+\; \frac{a}{6}[\bar{2}11]}_{b_r} \qquad (3)$$

Leading   Trailing   Twinning   Twinning

By incorporation, the approaching dislocation cross-slips onto the interface. The twinning partials (the residual dislocations, b_r) continue to glide in opposite directions, resulting in the twin migration (i.e. growth/shrinkage of a twin). The initial b_r provides additional resistance to new oncoming dislocations.

(b) Transmission

In Fig. 9(b), an oncoming pair of partial dislocations (a/6[$2\bar{1}1$] and a/6[112]) intercepts the twin boundary and transmits inside the twin. A sessile Frank partial type residual dislocation is left behind on the interface. Equation (4) summarizes the interaction.
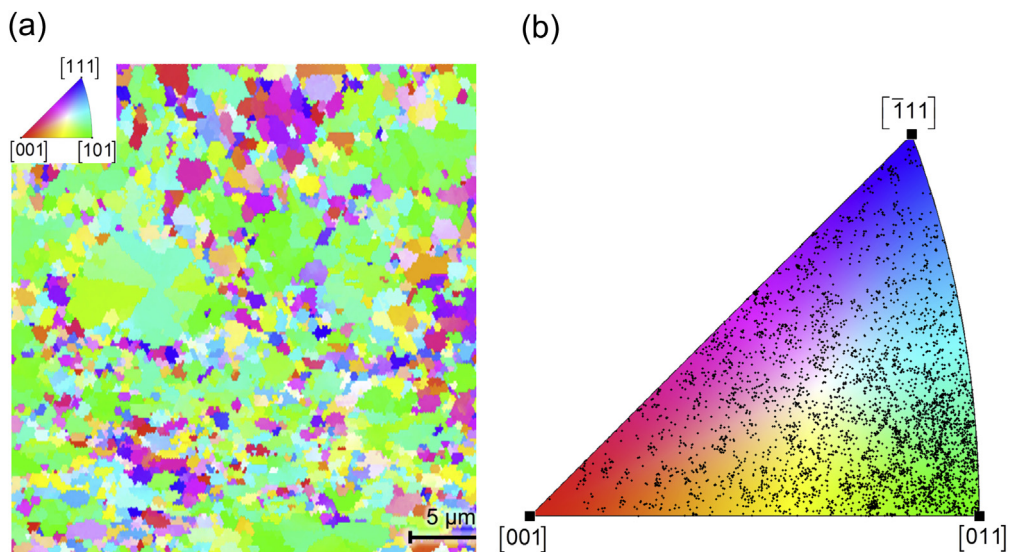

Fig. 4. (a) The grain orientation map of Ni-1% Co alloy from EBSD (Sangid et al., 2011). (b) Distribution of grain orientation superimposed on the stereographic triangle.
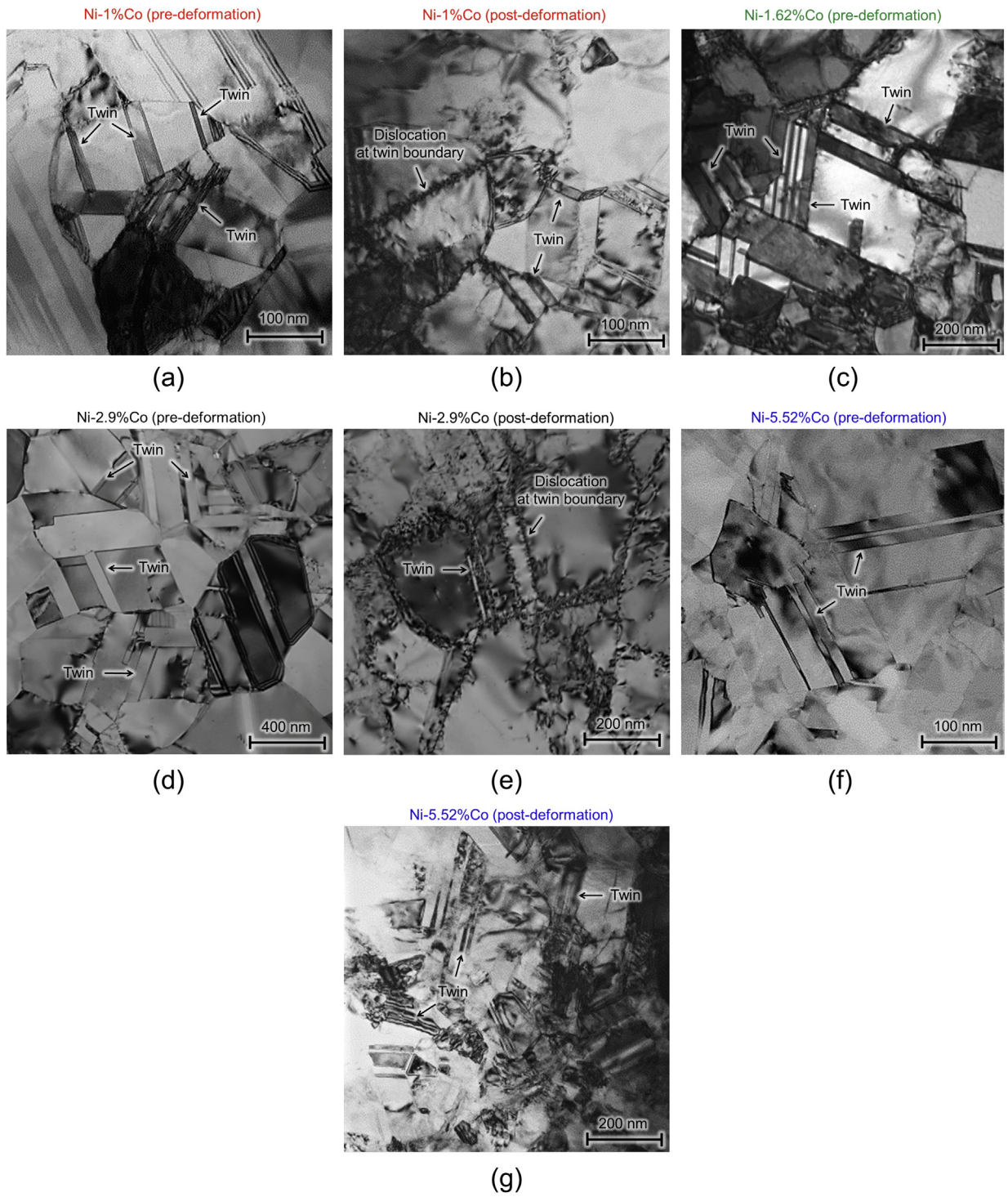
Fig. 5. TEM images demonstrating the widespread presence of nano-scale annealing twins. Notice the lack and the presence of dislocations at the twin boundaries before and after plastic deformation, respectively.
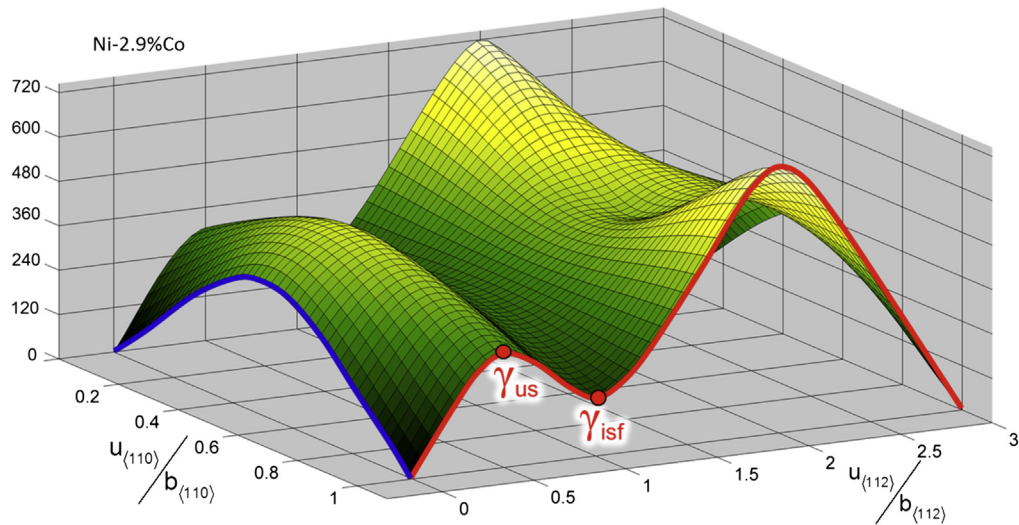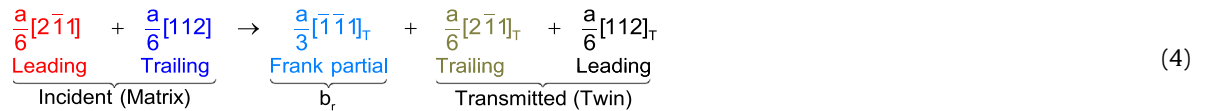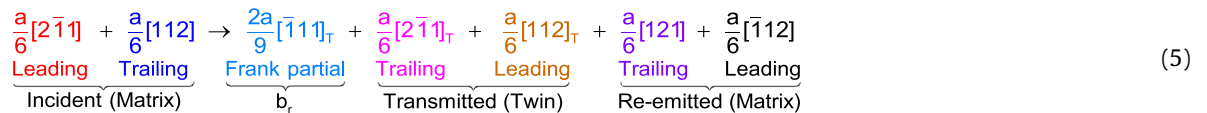
Fig. 6. A cutaway view of a single slip plane from the {111} family in an fcc lattice structure onto which dislocation slip occurs for the fcc crystal lattice.

$$\underbrace{\frac{a}{6}[2\bar{1}1] + \frac{a}{6}[112]}_{\substack{\text{Leading} \quad \text{Trailing} \\ \text{Incident (Matrix)}}} \rightarrow \underbrace{\frac{a}{3}[\bar{1}\bar{1}1]_T}_{\substack{\text{Frank partial} \\ b_r}} + \underbrace{\frac{a}{6}[2\bar{1}1]_T + \frac{a}{6}[112]_T}_{\substack{\text{Trailing} \quad \text{Leading} \\ \text{Transmitted (Twin)}}} \tag{4}$$

The newly approaching dislocations interact with the Frank partial and further slip nucleation at the reaction site ensues.

(c) Multiplication

Fig. 9(c) illustrates the nucleation of new dislocations i.e. the multiplication process. An extended dislocation intercepts the twin, and constricts into a full dislocation on the twin boundary. With favorable Schmid factors the interface, incident and outgoing slip systems (Table 3), the constricted dislocation disintegrates into two more extended dislocations − one inside the twin ($a/6[2\bar{1}1]_T$ and $a/6[112]_T$) and one re-emitting into the matrix ($a/6[121]$ and $a/6[\bar{1}12]$) as in Equation (5).

$$\underbrace{\frac{a}{6}[2\bar{1}1] + \frac{a}{6}[112]}_{\substack{\text{Leading} \quad \text{Trailing} \\ \text{Incident (Matrix)}}} \rightarrow \underbrace{\frac{2a}{9}[\bar{1}11]_T}_{\substack{\text{Frank partial} \\ b_r}} + \underbrace{\frac{a}{6}[2\bar{1}1]_T + \frac{a}{6}[112]_T}_{\substack{\text{Trailing} \quad \text{Leading} \\ \text{Transmitted (Twin)}}} + \underbrace{\frac{a}{6}[121] + \frac{a}{6}[\bar{1}12]}_{\substack{\text{Trailing} \quad \text{Leading} \\ \text{Re-emitted (Matrix)}}} \tag{5}$$
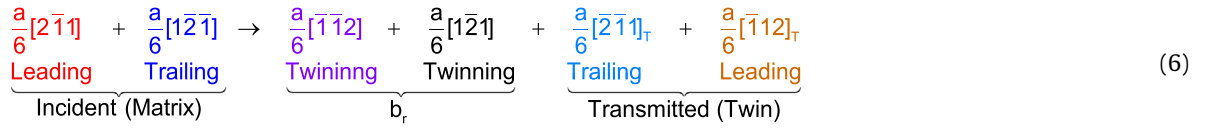
(d) Transmission and incorporation

In Fig. 9(d), when the oncoming leading partial $a/6[2\bar{1}1]$ impinges on the matrix–twin interface, a Shockley partial $a/6[\bar{1}12]_T$ is emitted inside the twin along with a twinning partial $a/6[1\bar{2}1]$. Once the trailing partial $a/6[1\bar{2}1]$ catches up, another twinning partial $a/6[\bar{1}12]$ and Shockley partial $a/6[\bar{2}\bar{1}1]_T$ (inside the twin) is generated. The interaction is summarized in Equation (6).

Table 2
First principles fault energy parameters (thus-computed unstable stacking fault energy represents the bulk value, i.e. the γ_{us}^{bulk}).

	Intrinsic stacking fault energy, γ_{isf} (mJ/m^2)	Unstable stacking fault energy, γ_{us} (mJ/m^2)
Pure Ni	128	254
Ni-1% Co	139	275
Ni-1.62% Co	143	287
Ni-2.9% Co	153	305
Ni-5.52% Co	149	297

$$\underbrace{\underbrace{\frac{a}{6}[2\bar{1}\bar{1}]}_{\text{Leading}} + \underbrace{\frac{a}{6}[1\bar{2}\bar{1}]}_{\text{Trailing}}}_{\text{Incident (Matrix)}} \rightarrow \underbrace{\underbrace{\frac{a}{6}[\bar{1}\bar{1}2]}_{\text{Twininng}} + \underbrace{\frac{a}{6}[1\bar{2}1]}_{\text{Twinning}}}_{b_r} + \underbrace{\underbrace{\frac{a}{6}[\bar{2}\bar{1}1]_T}_{\text{Trailing}} + \underbrace{\frac{a}{6}[\bar{1}12]_T}_{\text{Leading}}}_{\text{Transmitted (Twin)}} \tag{6}$$

(e) Blockage by Lomer lock formation

In Fig. 9(e), when the leading Shockley partial a/6[$\bar{2}$1$\bar{1}$] impinges on the boundary, it creates a Lomer dislocation a/2[101]$_T$. As the trailing partial catches up, a sessile stair rod dislocation a/3[100]$_T$ is generated in the vicinity of the Lomer lock. The overall reaction can be summarized as follows in Equation (7).
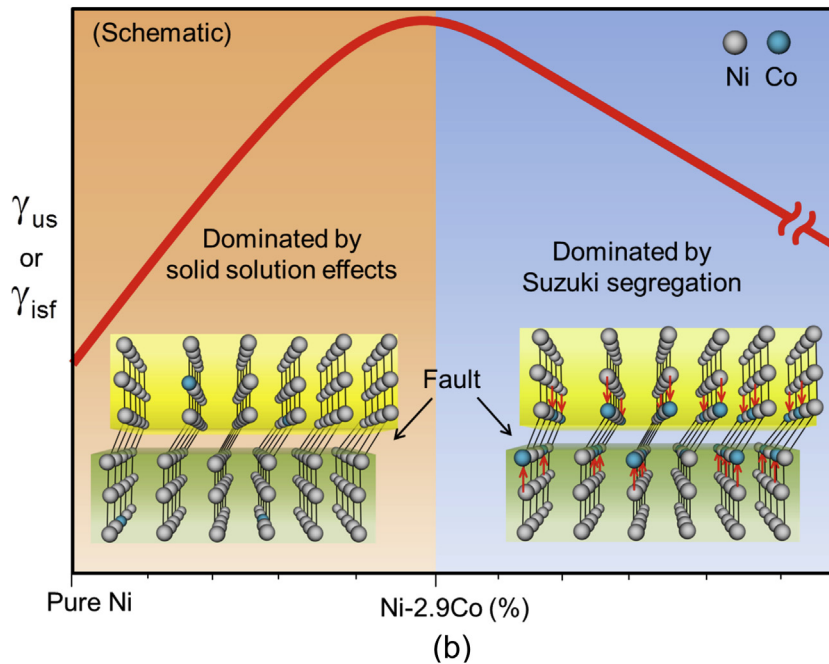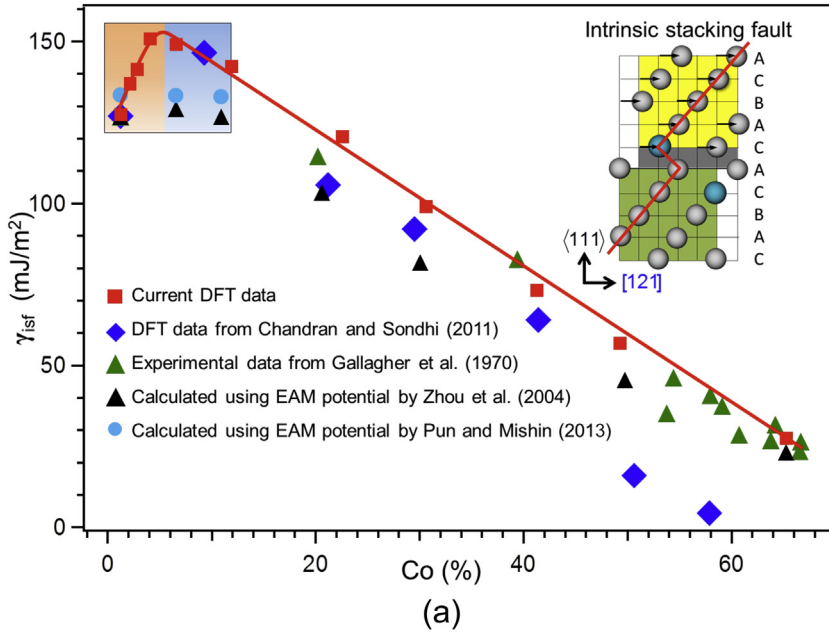

Fig. 7. (a) Comparison of the intrinsic stacking fault energy (γ_{isf}) from various sources. (b) The mechanistic origin of the non-uniform variation in the γ_{isf} and γ_{us} values at low Co content regime.

Table 3
Summary of slip-twin boundary interactions, the applied stress states and the Schmid factors, m on the partial dislocation of type a/6⟨112⟩ .

	Incorporation	Transmission	Multiplication	Transmission-incorporation	Blockage by Lomer lock
Stress state	$\begin{bmatrix} 0 & \sigma_{xy} & 0 \\ \sigma_{yx} & 0 & 0 \\ 0 & 0 & 0 \end{bmatrix}$	$\begin{bmatrix} 0 & 0 & \sigma_{xz} \\ 0 & 0 & 0 \\ \sigma_{zx} & 0 & \sigma_{zz} \end{bmatrix}$	$\begin{bmatrix} 0 & 0 & \sigma_{xz} \\ 0 & 0 & 0.5\sigma_{yz} \\ \sigma_{zx} & 0.5\sigma_{yz} & 0 \end{bmatrix}$	$\begin{bmatrix} 0 & \sigma_{xy} & 0 \\ \sigma_{xy} & 0 & 0 \\ 0 & 0 & \sigma_{zz} \end{bmatrix}$	$\begin{bmatrix} 0 & 0 & 0 \\ 0 & \sigma_{yy} & 0 \\ 0 & 0 & 0 \end{bmatrix}$
Incident dislocation (full) type	Screw	Edge	Mixed	Mixed	Mixed
$m_{incident}$	0.39	0.41	0.34	0.46	0.31
$m_{boundary}$	0.5	0.00	0.22	0.5	0.00
$m_{outgoing}$	–	0.41	0.34	0.46	0.16

$$\underbrace{\frac{a}{6}[\bar{2}1\bar{1}] + \frac{a}{6}[\bar{1}21]}_{\text{Incident (Matrix)}} \rightarrow \underbrace{\frac{a}{2}[101]_T + \frac{a}{3}[100]_T}_{b_r}$$

Leading   Trailing   Lomer   Stair rod

(7)

Unlike incorporation, the Lomer lock-induced blockage precludes any glissile activity on the twin boundary. Further slip incidence generates sufficiently high local stress to cause disintegration of the sessile dislocations.

4.3. Fault energetics of slip-boundary interactions

Due to different magnitudes of residual dislocation $\vec{b}_r = \vec{b}_{incoming} - \vec{b}_{transferred}$ various degrees of local stress concentration is imposed on the twin boundary (Fig. 10). The magnitude of the residual dislocation is $b_r = \sqrt{b_1^2 + b_2^2 + b_3^2}$ when, $\vec{b}_r = b_1\ \hat{x} + b_2\ \hat{y} + b_2\ \hat{z}$, and b_1, b_2 and b_3 are vector component values and $\hat{x}$, $\hat{y}$, $\hat{z}$ are orthonormal unit vectors in the crystallographic directions. Using the method described in Appendix B, we compute the values of γ_{us} for different interactions as a function of the number of impinging dislocations, N, and the magnitude of residual slip, b_r (Fig. 11). To illustrate the cause-and-effect relationship among the parameters − γ_{us}, b_r and N, the data from Fig. 11 are presented separately in Fig. 12(a) and (b). It can be noted from Fig. 12(a) that the magnitudes of the residual Burgers vector, b_r, eventually leads to saturated levels (denoted by b_r^{sat}), regardless of the reaction type with increasing number of oncoming dislocations.

4.3.1. Evolution of γ_{us} during slip−boundary interactions

The apparent saturation occurs due to the dissociation of the b_r with increased slip impingement. The dissociated b_r shifts from the original reaction site, thereby offering no stress concentration to the newly approaching slip. One can recall that the stress concentrations associated with a b_r is extremely localized. Hence, the dissociation/relocation of the b_r precludes any stress contribution towards increasing the γ_{us} value for the approaching slip. The details differ for individual reaction cases. However, the fundamental mechanistic process is essentially similar.

The maximum (at saturation) elevation in the γ_{us} due to Lomer lock formation is as high as 1957.2 mJ/m^2 (denoted by γ_{us}^{sat}). The saturated energy barrier for incorporation, γ_{us}^{sat}, is calculated to be the lowest of all the reactions in the current study (474 mJ/m^2). We note that the fault energy barrier associated with incorporation process is traditionally designated as "unstable twinning energy barrier" (γ_{ut}) (Ogata et al., 2002) as incorporated glide is essentially equivalent to a twin migration process. However, for the sake of simplicity, we treat the peak γ energy barrier during the glide of the twinning partial (i.e. the incorporated Shockley partial) as the γ_{us} in the present study.

### 4.4. Prediction of critical flow stresses

4.4.1. Free glide strength, $\tau_{free\ glide}$

We employ Peierls-Nabarro (PN) model (Nabarro, 1947; Peierls, 1940) to convert the γ_{us} energies into frictional stresses (Fig. 13(a)). The total energy expenditure during dislocation glide (also known as the misfit energy, E_{misfit}) is a function of γ_{us} and the disregistry function $f_{disregistry}$. Using the bulk energy barrier γ_{us}^{bulk}, the free glide strength $\tau_{free\ glide}$ for a dislocation can be computed from Equation (8) (Hirth and Lothe, 1982; Joos et al., 1994; Schoeck, 1994).

$$\tau_{free\ glide} = max\left\{\frac{1}{b}\frac{\partial E_{misfit}\left(f_{disregistry}, \gamma_{us}^{bulk}\right)}{\partial u}\right\} \tag{8}$$

where, u is the dislocation location and the Burgers vector magnitude, $b = \left|\vec{b}\right| = a/\sqrt{6}$.

The $f_{disregistry}$ represents the horizontal displacement differential of the atoms (before and after the occurrence of slip) across the slip plane, and hence captures the elastic distortion surrounding the dislocation core (Joos et al., 1994; Schoeck, 1994). The disregistry function, $f_{disregistry}$ for an extended dislocation with partial splitting distance, d_{split}, is given by Equation (9) (Schoeck, 1994, 2005).
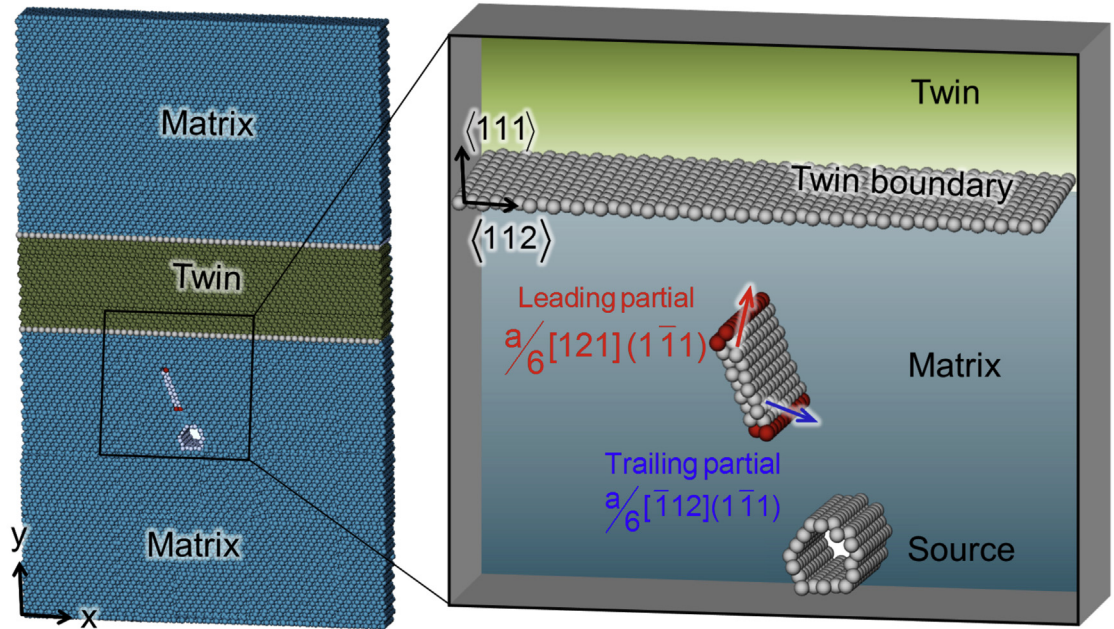
(a)
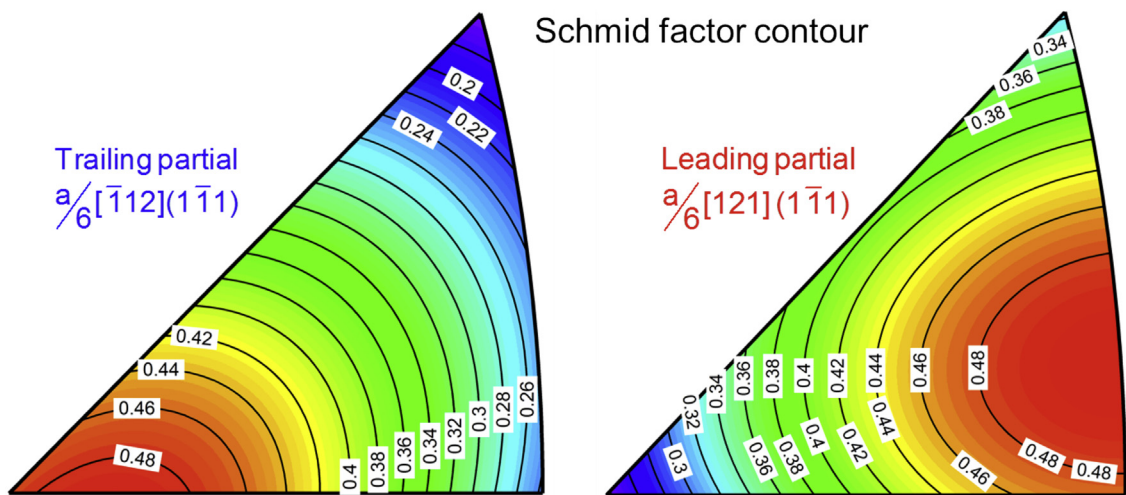
(b)

Fig. 8. (a) Molecular dynamics simulation of a single nano-twinned grain to study various slip-twin boundary interaction mechanisms. (b) Variation of Schmid factor on leading/trailing dislocations depending on the crystal orientation.
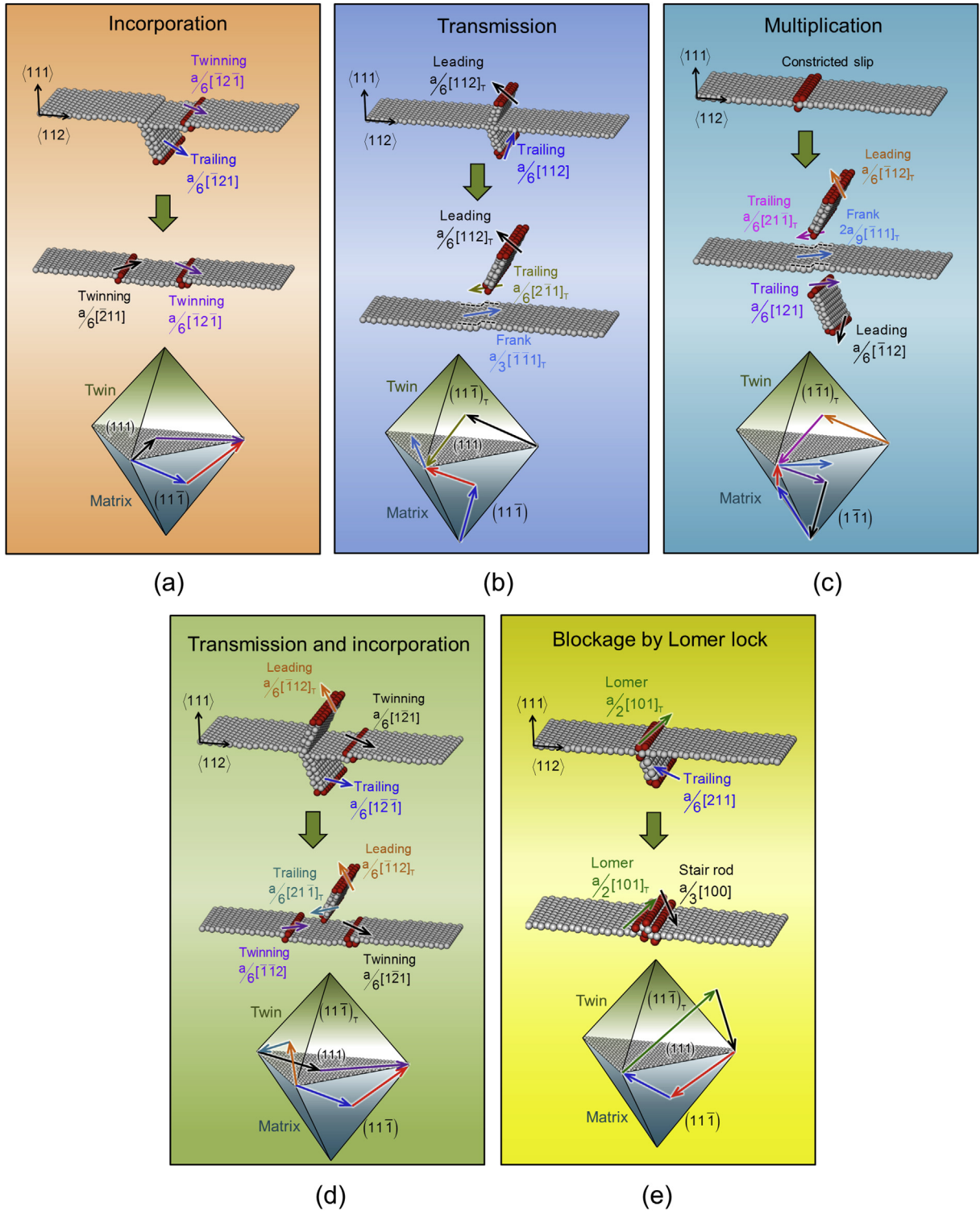
Fig. 9. (a) Incorporation of slip on twin boundary interactions. (b) Transmission of oncoming slip past a coherent twin boundary. (c) Multiplication of dislocations following the interception of the twin boundary by a matrix dislocation. (d) Simultaneous occurrence of transmission and incorporation of the impinging slip from the source in the matrix. (e) Blockage of the oncoming slip by the formation of Lomer lock (in conjunction with stair rod dislocation).
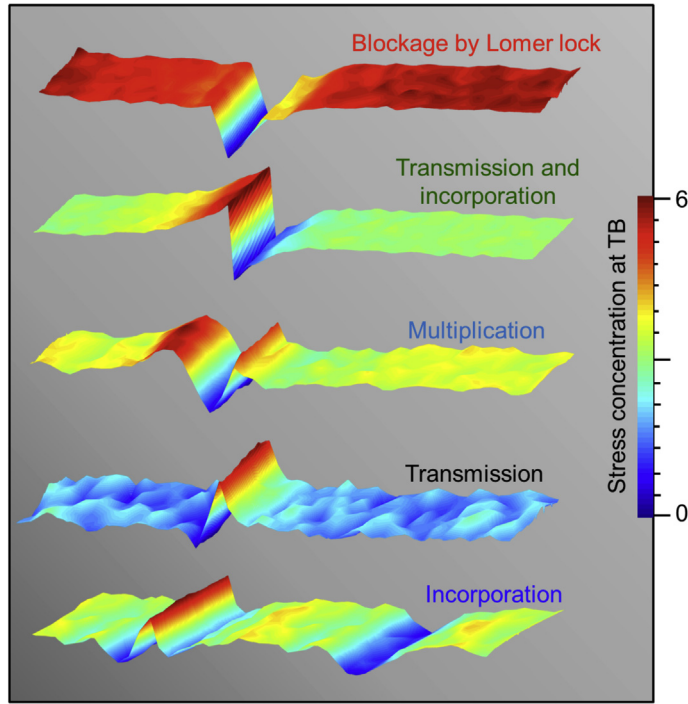
Fig. 10. Stress concentration distribution on the twin boundary following the very first incidence of the matrix dislocation.

$$f_{\text{disregistry}} = b + \frac{b}{\pi} \left[\tan^{-1} \left(\frac{ma' - u}{\zeta} \right) + \tan^{-1} \left(\frac{ma' - u - d_{\text{split}}}{\zeta} \right) \right] \qquad (9)$$

where, m is an integer ranging from $-\infty$ to $+\infty$, which accounts for the long range of $f_{\text{disregistry}}$ (for numerical calculation, m is assumed to be a large number); a' is the lattice periodicity i.e. shortest distance between two equivalent atomic rows in the Burgers vector direction i.e. $a' = 2b = 2a/\sqrt{6}$; ζ the core half-width of the individual partial ($\zeta_{\text{screw}} = a/2\sqrt{3}$ and $\zeta_{\text{edge}} = a/2\sqrt{3}(1-\upsilon)$; υ is Poisson's ratio).

The E_{misfit} denotes the area underneath the γ surface, and can be written as a Frenkel type expression (Hirth and Lothe, 1982; Joos et al., 1994; Schoeck, 1994): $E_{\text{GSFE}} = \sum \gamma(f_{\text{disregistry}}, \gamma_{\text{us}}) \, a'$ as in Equation (10).
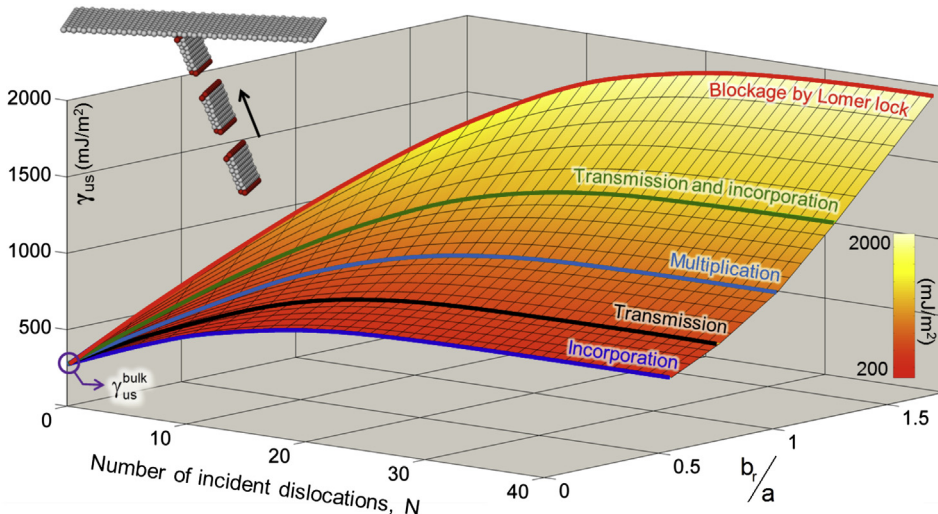

Fig. 11. Evolution of the unstable stacking fault energy (γ_{us}) from the bulk magnitude to the higher values at the site of the slip–interaction reactions.
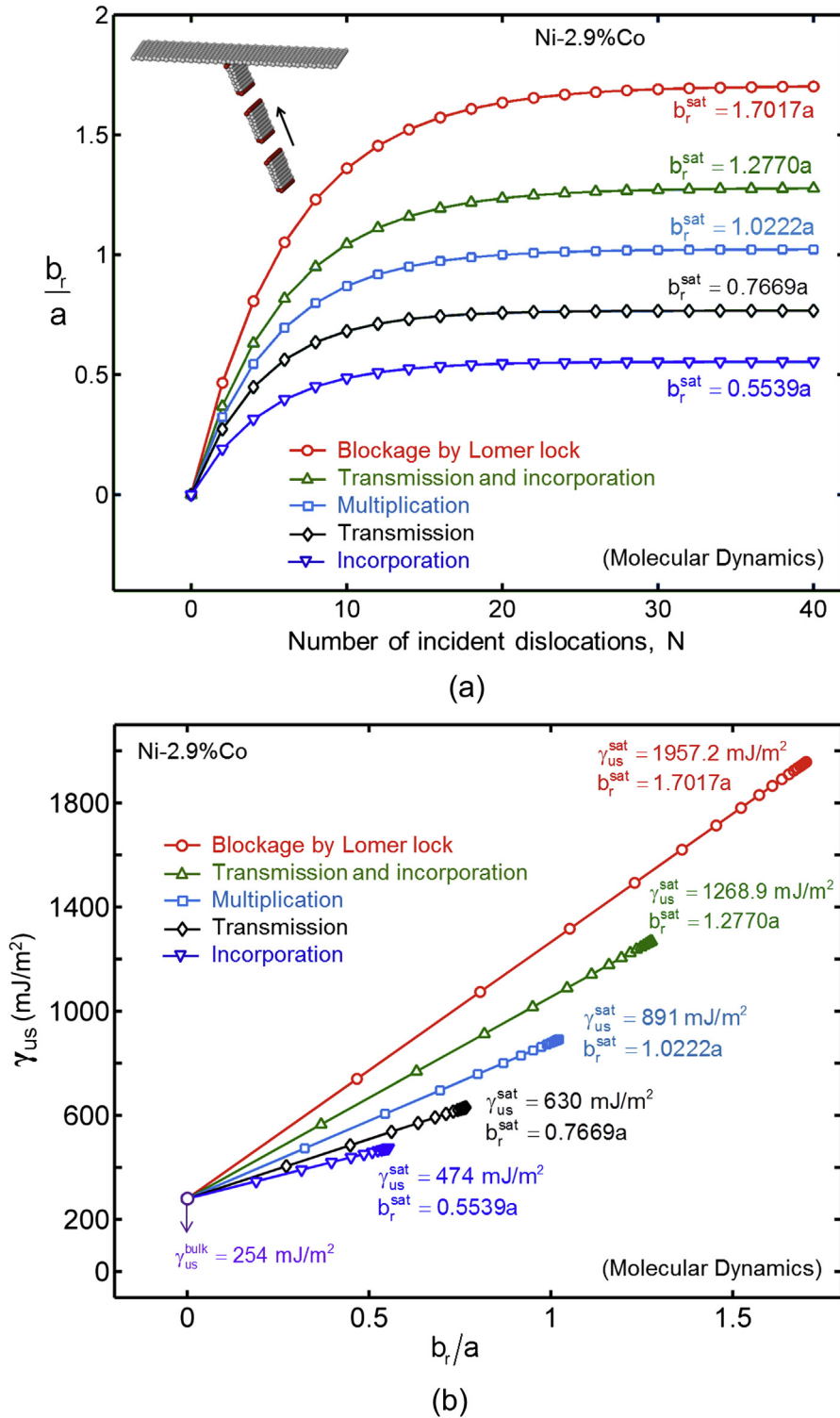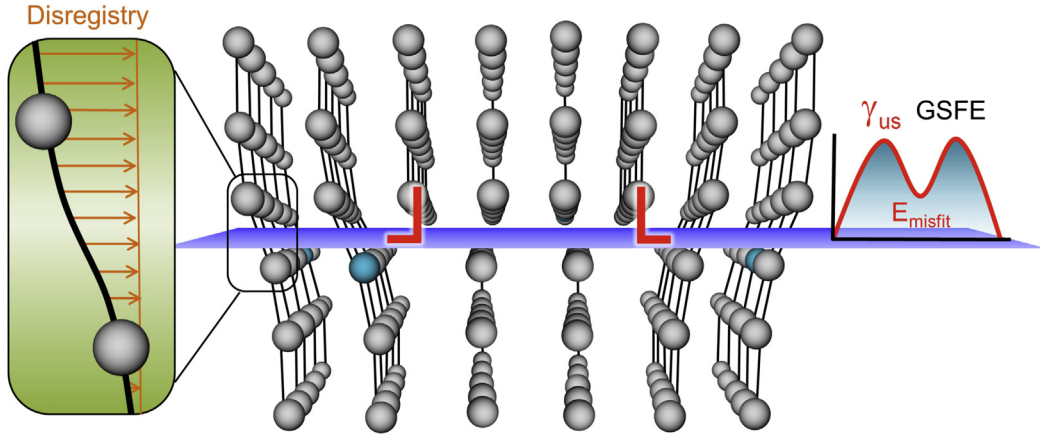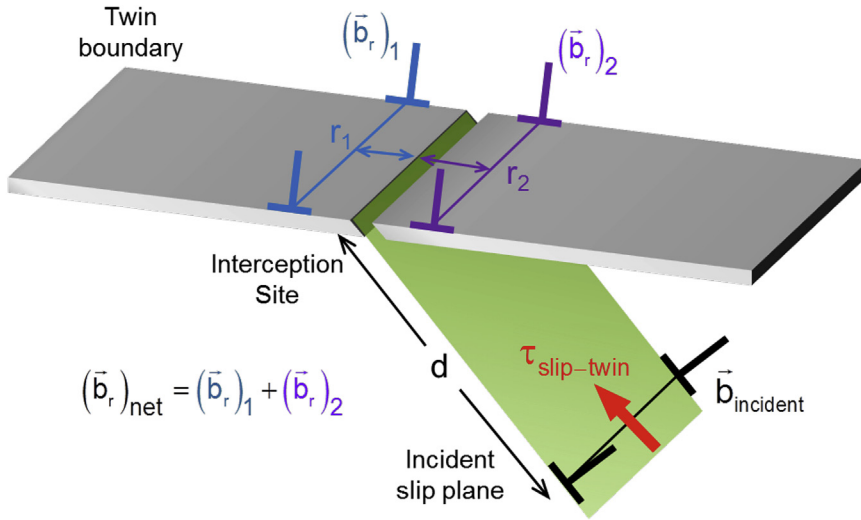
(a)

(b)

Fig. 12. (a) Variation in the magnitude of the total residual dislocation at the interface with increasing incidence events. (b) The linear correlation between the γ_{us} and the residual Burgers vector, $\overline{b}_r$.

(a)

(b)

Fig. 13. (a) The disregistry and the GSFE are the two essential ingredients in predicting frictional stress within Peierls-Nabarro formalisms. (b) The model configuration for calculating the slip-twin interaction strength, $\tau_{\text{slip−twin}}$ in the presence of the net residual slip $(\vec{b}_r)_{\text{net}} = (\vec{b}_r)_1 + (\vec{b}_r)_2$.

$$E_{\text{misfit}}\left(f_{\text{disregistry}}, \gamma_{\text{us}}\right) = 2\underbrace{\sum_{m=-\infty}^{m=+\infty}\left[\gamma_{\text{us}}\sin\frac{\pi f_{\text{disregistry}}}{b}\right]\frac{b}{2}}_{\text{GSFE for } 0 \leq u/b \leq 0.5} + 2\underbrace{\sum_{m=-\infty}^{m=+\infty}\left[\frac{\gamma_{\text{us}} + \gamma_{\text{isf}}}{2} - \frac{\gamma_{\text{us}} - \gamma_{\text{isf}}}{2}\sin\frac{\pi f_{\text{disregistry}}}{b}\right]\frac{b}{2}}_{\text{GSFE for } 0.5 < u/b \leq 1} \tag{10}$$

Equation (10) represents a generic expression, wherein any magnitude of γ_{us}(e.g. for the free glide and/or the obstructed glide) can be inserted to obtain the corresponding misfit energy level.

4.4.2. Slip-twin boundary interaction strength, $\tau_{\text{slip−twin}}$

Fig. 13(b) illustrates the current approach of computing the $\tau_{\text{slip−twin}}$. The presence of accumulating $\vec{b}_r$ leads to two distinct forms of energy expenditure for the newly approaching slip to overcome − (a) the aforementioned misfit energy, $E_{\text{misfit}} = E_{\text{misfit}}(\gamma_{\text{us}})$, and (b) the $\vec{b}_r$ induced elastic energy, $E_{\text{residual}} = E_{\text{residual}}(b_r)$. The applied stress $\tau_{\text{slip−twin}}$ required to move the oncoming dislocation towards the boundary by a distance of ∂d can be derived from the work-energy balance as in Equation (11).

$$\underbrace{b_{\text{incident}}\tau_{\text{slip-twin}}\partial d}_{\text{work done}} = \underbrace{\partial E_{\text{misfit}}\left(f_{\text{disregistry}}, \gamma_{\text{us}}\right) + \partial E_{\text{residual}}(b_r)}_{\text{energy expense}} \tag{11}$$

Due to high local stress (on the twin boundary) as a result of accumulation, individual $\vec{b}_r$ are located at different positions from the initial site. Fig. 13 considers the case of the net $\vec{b}_r$ comprising, for example, two component residual dislocations — $(\vec{b}_r)_1$ and $(\vec{b}_r)_2$ located at r_1 and r_2 distances away from the original interception site as indicated. Based on the work-energy balance in Equation (11), we propose the generic expression of the $\tau_{\text{slip-twin}}$ for any number of component residual dislocation $(\vec{b}_r)_i$ located at r_i (i = 1, 2, 3…) as in Equation (12).

$$\tau_{\text{slip-twin}} = \max\underbrace{\left\{\frac{1}{b_{\text{incident}}}\frac{\partial E_{\text{misfit}}\left(f_{\text{disregistry}}, \gamma_{\text{us}}\right)}{\partial u}\right\}}_{\text{short range (misfit)}} + \underbrace{\frac{1}{db_{\text{incident}}}\sum_i \frac{\mu(b_r)_i^2}{4\pi}\ln\left(\frac{R}{r_i}\right)}_{\text{long range (elastic)}} \tag{12}$$

where, R is the size of the grain containing the twin and μ the shear modulus. The R/r_i ratios are assumed to be constant at a magnitude of 1/500, considering the fact that such a value amounts to the summation of the classical strain energy expressions of the residual dislocations i.e. $\sum_i \frac{\mu(b_r)_i^2}{2}$ (Hirth and Lothe, 1982).

For the current calculations, we deem it reasonable to assume the magnitudes of "d" to be on the order of tens of nanometers (from 10 to 20 nm). Clearly, this parameter in reality will be decided by the twin spacing as well as the dislocation source density. It is rather challenging to establish this parameter experimentally. Hence, to assume realistic values (in accordance with the TEM observations), we adhere to the magnitudes which correspond to the nano-dimensions of the twins in the TEM pictures as well as predicts a reasonable $\tau_{\text{slip-twin}}$ level. It is important to note that the assumption of "d" values does not necessarily alter the fundamental aspect of the modeling.

Equation (12) can be used to predict the slip transfer strength, $\tau_{\text{slip-twin}}$ corresponding to any particular mechanisms by inserting the saturated values of b_r (i.e. the b_r^{sat}), and the unstable stacking fault energy value i.e. $\gamma_{\text{us}}^{\text{sat}}$. The calculated values are presented in Table 4.

4.4.3. Prediction of τ_{CRSS} for different Ni–Co alloys

First, we propose a suitable extrapolation strategy to obtain various $\tau_{\text{slip-twin}}$ levels for all Ni–Co alloys. Based on simulating Ni-2.9% Co as the representative material, the γ_{us} is found to be a linear function of the b_r. It is quite reasonable to assume that the other Ni–Co alloys would undergo similar reaction mechanisms, and hence essentially yield similar $\gamma_{\text{us}} - b_r$ correlation. Therefore, we propose a simple linear relation in the form of Equation (13) to predict the energy barrier levels in various alloys. In doing so, each alloy differs in terms of the composition-dependent bulk $\gamma_{\text{us}}^{\text{bulk}}$ values computed from first principles (Table 2). Such an approach is particularly advantageous, in that it circumvents repeating the same set of MD reaction simulations on each alloy (which is clearly a superfluous measure).

$$\gamma_{\text{us}} = \underbrace{M_{\text{reaction}}b_r/a}_{\text{from MD}} + \underbrace{\gamma_{\text{us}}^{\text{bulk}}}_{\text{from DFT}} \tag{13}$$

where, M_{reaction} is the slope of γ_{us} versus b_r curves in Fig. 12(b) for each reaction: $M_{\text{incorp}} = 352.05 \text{ mJ/m}^2$, $M_{\text{trans}} = 457.55 \text{ mJ/m}^2$, $M_{\text{multi}} = 598.53 \text{ mJ/m}^2$, $M_{\text{trans-incorp}} = 774.47 \text{ mJ/m}^2$, $M_{\text{Lomer}} = 985.31 \text{ mJ/m}^2$. Now, by inserting the $\gamma_{\text{us}}^{\text{bulk}}$ from Table 2 and the appropriate M_{reaction} and b_r^{sat} for a particular reaction mechanisms in Equation (13), we extrapolate the corresponding $\gamma_{\text{us}}^{\text{sat}}$ values for all Ni–Co alloys. These new $\gamma_{\text{us}}^{\text{sat}}$ magnitudes in turn are input into Equation (12) to predict the corresponding $\tau_{\text{slip-twin}}$ levels (Table 4).

Table 4
Peierls-Nabarro model based strength of slip transfer mechanisms past a twin boundary $\tau_{\text{slip-twin}}$ and free glide strength (i.e. Peierls stress) $\tau_{\text{free glide}}$ in different Ni–Co alloys.

	$\tau_{\text{free glide}}$ (MPa)	$\tau_{\text{slip-twin}}$ (MPa)				
	Free glide	Incorporation	Transmission	Multiplication	Transmission-incorporation	Lomer lock formation
Ni-1% Co	33	153	198	245	297	393
Ni-1.62% Co	48	161	213	253	306	411
Ni-2.9% Co	60	175	230	280	336	445
Ni-5.52% Co	55	166	219	269	321	423

To predict the τ_{CRSS} for the current nano-twinned alloys, we consider three major microscopic flow contributions — (a) the free glide stress $\tau_{free\ glide}$, (b) slip-twin boundary interaction stress, $\tau_{slip-twin}$, and (c) the forest hardening stress (at a pre-deformation dislocation density) $\tau_{forest} = \alpha\mu b\sqrt{\rho}$ (Estrin and Mecking, 1984; Jackson and Basinski, 1967); where α is a material constant (from 0.5 to 1) and ρ the forest dislocation density (assumed to be $10^{14}/m^2$ which is the typical pre-deformation literature value). The $\tau_{slip-twin}$ is observed to be the most dominating term. Using Equation (14), we calculate the τ_{CRSS} levels for different Ni–Co alloys based on the iso-strain type mixing formulations.

$$\tau_{CRSS} = \left(1 - V_f\right)\tau_{free\ glide} + \sum_{reaction} V_f^{reaction}\tau_{slip-twin}^{reaction} + \left(1 - V_f\right)\tau_{forest} \tag{14}$$

where, V_f is the total volume fraction of the material region hosting the aggregate slip-twin reactions; $V_f^{reaction}$ is the assigned volume fraction for a specific reaction i.e. $V_f = \sum_{reaction} V_f^{reaction}$. The $V_f^{reaction}$ value to a particular reaction is assigned on the basis of the fact that the EBSD results demonstrated only a mild texture (almost close to random distribution of grains) in Fig. 4(a) and (b). Hence, we assume that the MD-observed stain transfer mechanisms would occur with equal frequency/probability. Therefore, for the modeling purpose, an equal volumetric contribution of the all five categories of the slip transfer mechanisms is considered in Equation (14). The values of the τ_{CRSS} for the current Ni–Co alloys are predicted and compared with experimentally determined τ_{CRSS} in Fig. 14.

5. Discussion

5.1. Role of composition

The role of the Ni–Co composition has been identified as particularly influencing the fault energetics at the atomic scale. Early literature (Beeston et al., 1968; Gallagher, 1970; Howie and Swann, 1961) note that the intrinsic stacking fault energy γ_{isf} values of Ni–Co alloys undergo a gradual reduction with increasing Co content from the pure Ni level. Through quantum mechanical calculations, we report the presence of a non-uniform trend at low Co concentration. Recent theoretical literature also report similar findings on the Ni–Co γ_{isf} levels (Chandran and Sondhi, 2011; Zhang et al., 2013). We trace the origin of such trend to an atomic level competition between the solid solution hardening effects and the solute segregation (known as the so-called Suzuki segregation). Suzuki first reported the experimental
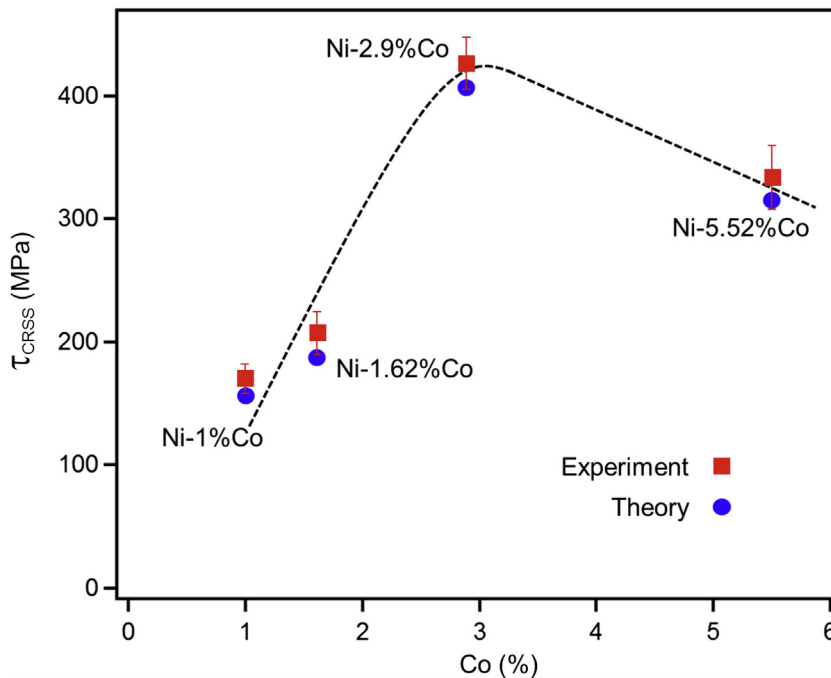

Fig. 14. Comparison between the predicted and experimentally determined τ_{CRSS} levels for different Ni–Co alloys.

evidence of the role of solute segregation on reducing the fault energetics (Suzuki, 1962). Starting from pure Ni up to a Co content of 2.9% (by weight), the gradual rise in the fault energy levels (both γ_{us} and γ_{isf}) is observed to be dominated by solid solution hardening. Throughout the rising portion of the curve, the Co solutes continue to create enhanced resistance for lattice shearing. On reaching the peak magnitude (at 2.9% Co), the solute drag effects are eventually overwhelmed by the Suzuki segregation effects, leading to the dip of the curve. The evidence of a decrease in the fault energies due to the solute segregation is also reported in the recent literature (Apostol and Mishin, 2011; Koizumi et al., 2012).

Now, questions may arise regarding whether the observed trend in the Co-influenced γ surface are indeed representative of the inherent material properties. Specifically, one must check the sensitivity of: (a) the energy relaxation procedure, (b) the positioning of solutes, and (c) the simulation supercell size.

We have investigated the role of different relaxation methods (Ngan, 1995) – (i) the full relaxation (when atomic positions are allowed to adjust in all directions), (ii) "the vertical relaxation" (when atoms adjust positions only vertical to the fault plane), and (iii) no relaxation whatsoever. In doing so, the maximum variation was limited to ± 4 mJ/m^2 both in the levels of γ_{isf} and γ_{us}, assuring the accuracy of our results. Secondly, various positioning of the solute atoms results only in a variation of ± 3 mJ/m^2. The physical origin of such insensitivity can be attributed to the strong similarity between the Co and Ni atoms discussed as follows.

Typically in metallic alloys, the addition of the substitutional solute atoms of different elements to the base metal matrix results in the lattice distortion and the change in bonding landscape. The lattice distortion depends on the volumetric mismatch among the constituent elements while bonding landscape is decided by the electronic configurations. Other important factors are the chemical potential and the magnetic properties of each element. All these variables would essentially factor in the nature and magnitudes of the alloy γ surface. For instance, the mixing of two elements, which are very dissimilar in terms of the atomic volumes, would result in a large lattice distortion and hence higher sensitivity to the solute positioning with respect to the fault. Likewise, the magnetism of the constituent atoms (which is in fact dictated by the nature of electronic spin at the outermost shells in individual atoms) would impart a profound influence on the fault energetics. However, for the Ni–Co binary alloys, both Ni and Co are transitional metals, which possess very similar physical attributes in terms of the atomic volumes (the respective radii being 0.124 and 0.125 nm), the electronic configurations (Ni $\equiv$ [Ar] $3d^8\ 4s^2$ and Co $\equiv$ [Ar] $3d^7\ 4s^2$) and the magnetism (both being ferromagnetic). In other words, during alloying the Co solute atoms can substitute Ni atoms without creating a considerable disturbance in the base metal properties. Therefore, when the quantity of the Co solutes in the Ni matrix is only very minute, no significant change in the neighborhood of the Co solute atoms is noticed by the material. As a result, the role of Co solutes as the point defects would be negligible except for altering the electronic structure in the vicinity, thereby eliminating the aforementioned simulation artifacts.

In summary, the compositional dependence of the Ni–Co γ surface is demonstrably tuned with the trends in the experimental yield strengths. Given the fact that the γ surface governs the inherent slip characteristics, the overall tendency towards slip glide resistance at the mesoscale would differ considerably among the various Ni–Co alloys. Particularly, the presence of the nano-sized annealing twins would significantly enhance the composition-dependent slip characteristics within individual grains, thereby deciding the macroscopic hardening behavior.

5.2. Role of nano-twins

At the mesoscale, the coherent twin boundaries play the role of increasing the impedances to dislocation motion. Hence, the magnitudes of the critical resolved shear stress τ_{CRSS} of the Ni–Co alloys are decided by the presence of annealing twins. Particularly, we demonstrate the importance of considering different slip-twin boundary reactions in imparting various degrees of glide resistances. Hence, in the proposed theory, we have examined multiple types of reaction mechanisms to predict the relative $\tau_{slip-twin}$ levels for the respective mechanisms.

These reactions are triggered on the basis of: (a) the local stress state i.e. the relative Schmid factors on the twin boundary, incident, and outgoing slip systems, and (b) the geometry of the intercepting slip i.e. edge/screw/mixed (Lee et al., 1990). For a polycrystalline material, different local stress states at twin boundaries would arise from grain to grain. We note that the current reactions occur under the unique local stress state and the geometry of the incident slip (as summarized in Table 3). Further investigation of modifying either of these two variables, and the associated change in the mechanism would be one interesting future research. Earlier literature have addressed the details of individual reactions both theoretically and experimentally: (a) incorporation (Asaro and Kulkarni, 2008; Jin et al., 2006; Müllner and Solenthaler, 1997), (b) transmission (Kacher et al., 2014; Zhu et al., 2007), (c) multiplication (Miller et al., 2006), (d) transmission and incorporation (Evans, 1974; Jin et al., 2008; Mahajan and Chin, 1973), and (e) blockage by a Lomer lock formation (Karnthaler, 1978; Wang and Huang, 2006). The relative preference for these reactions bears important implications regarding the macroscopic strength and ductility. For example, the incorporation process can be deemed as a special case of slip blockage mechanism, which still permits straining along twin boundaries. Early literature (Zhu et al., 2007) note that the origin of considerable ductility in nano-twinned materials can be attributed to the pervasive incorporation process. On the other hand, a large number of grains favorably oriented for Lomer lock formation would contribute

to increased strengthening attributes. Similarly, multiplication and transmission–incorporation processes would play roles in both hardening and ductility to some extent. The currently predicted resistance stresses $\tau_{\text{slip–twin}}$ for various mechanisms hold considerable promise for the use in modeling further material properties such as the damage tolerance (Chowdhury et al., 2014b).

We note that a detailed exploration of further combinations of applied stresses (e.g. shear, tension etc.) on the nano-twinned grain (in the molecular dynamics simulations) would essentially differ only in terms of the local stress state. This, in turn, may culminate in other reactions types (or the currently reported ones with slight modifications depending again on the combination of the Schmid factors on incident/boundary/outgoing slip planes). That is why it is more convenient to categorize the slip-twin boundary reaction mechanisms in light of the Schmid factor scenario. It is because, for example, even apparently different global stress states may yield the same local resolved shear stresses on the respective systems, leading to the same slip transfer mechanisms. Hence, we resort to categorizing five different types which are also experimentally verified in earlier literature.

Now, the question may arise regarding what volume fraction of individual reactions prevails during the deformation. Intuitively, if a material is very strongly textured, the majority of grains will have the same orientations, and hence a predominant local stress state, which in turn will result in the prevalence of a particular reaction. On the other hand, a material with random/mild texture, which is the current case, is most likely to have an equal distribution of various slip transfer mechanisms. We note that it is rather challenging to experimentally establish the exact nature of slip transfer processes at twin boundaries in individual grains *in-situ*. For example, TEM methods can only probe sub-micron area. On the other hand, EBSD cannot reveal any interaction mechanisms on a grain by grain basis. Now, for the current Ni–Co alloys, even though the EBSD map indicates a mild texture, the Taylor factor for this material is computed to be 3.06 (Sangid et al., 2011), which in fact suggests the presence of a wide range of grain distribution. Therefore, it is quite reasonable to assume that the current set of reactions is likely to prevail with nearly equal probability.

6. Summary and conclusion

The major contributions of the present research are summarized below.

1) Constitutive responses of polycrystalline Ni–Co alloys are investigated via uniaxial tension experiments. Critical resolved shear stresses for Ni-1% Co, Ni-1.62% Co, Ni-2.9% Co and Ni-5.52% Co alloys are determined to be 170.6 MPa, 206.2 MPa, 426.2 MPa and 333.3 MPa respectively. The observations suggest the existence of a critical composition to achieve the maximum strength. TEM micrographs reveal a prevalence of nano-sized annealing twins in the alloys. On deformation, a substantial increase in dislocation density at the twin boundaries is evidenced, suggesting widespread slip-twin interactions contributing to macroscale strengths.

2) First principles calculations reveal that the compositional dependence is related with an atomic-scale competition between the solid solution hardening and the solute segregation. The γ surface values undergo a rise (controlled by solid solution hardening), and subsequently a fall (governed by solute segregation) with increasing Co content. The overall compositional trend in the alloy γ surface (i.e. γ_{us} and γ_{isf} values) is found to follow the same experimental trend as the alloy strengths.

3) Various strain transfer mechanisms past a coherent twin boundary have been studied using molecular dynamics simulations. Different residual dislocations are found to influence the extrinsic levels of the γ_{us}. A Peierls-Nabarro framework was employed to convert the extrinsic γ_{us} levels into the twin boundary penetration strengths for the corresponding strain transfer mechanisms. The computed boundary strengths are subsequently extrapolated for different alloy compositions. Critical resolved shear stresses (τ_{CRSS}) are predicted for the Ni–Co alloys in question.

4) Overall, the present theory suggests that the experimental differences in hardening behaviors originate from alloying-induced quantum level differences in the γ surfaces. Alterations in the fault energetics (owing to adding even minuscule amounts of substitutional Co atoms) can be considerably amplified at the mesoscale defect interaction level. As a result, the frictional stresses required for widespread dislocation interactions with twin boundaries would undergo augmented effects from one composition to another. Therefore, these discrete lattice level effects manifest themselves in the form of considerable differences in the macroscopic strengthening behaviors.

Appendix A. γ Surface from density functional theory

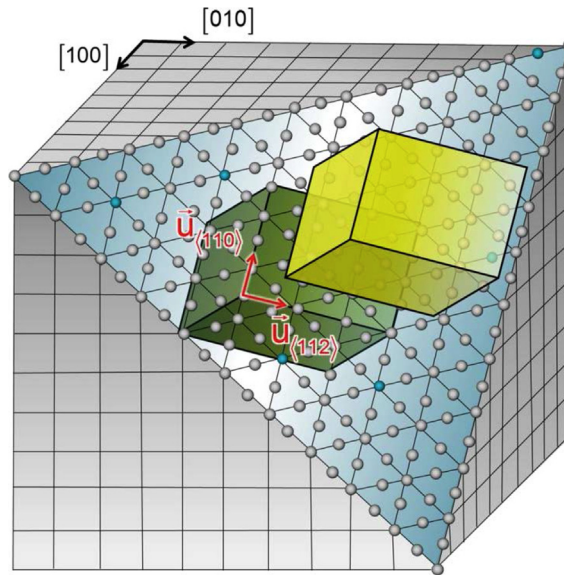**Fig. A1.** Two crystal blocks are rigidly shear-displaced on the (111) plane.

Fig. A1 illustrates the crystal configuration for calculating the γ surface in DFT simulations. Two crystal blocks adjoining each other on the (111) slip plane are rigidly sheared by the displacement vector, $\vec{u} = \vec{u}_{\langle 110 \rangle} + \vec{u}_{\langle 112 \rangle}$. The γ energy corresponds to the energy differential between the sheared structure and the original one ($E_{sheared} - E_{perfect}$) as normalized by the area (A) as in Equation (15) (Vitek, 1968).

$$\gamma = \frac{E_{sheared} - E_{perfect}}{A} \tag{15}$$

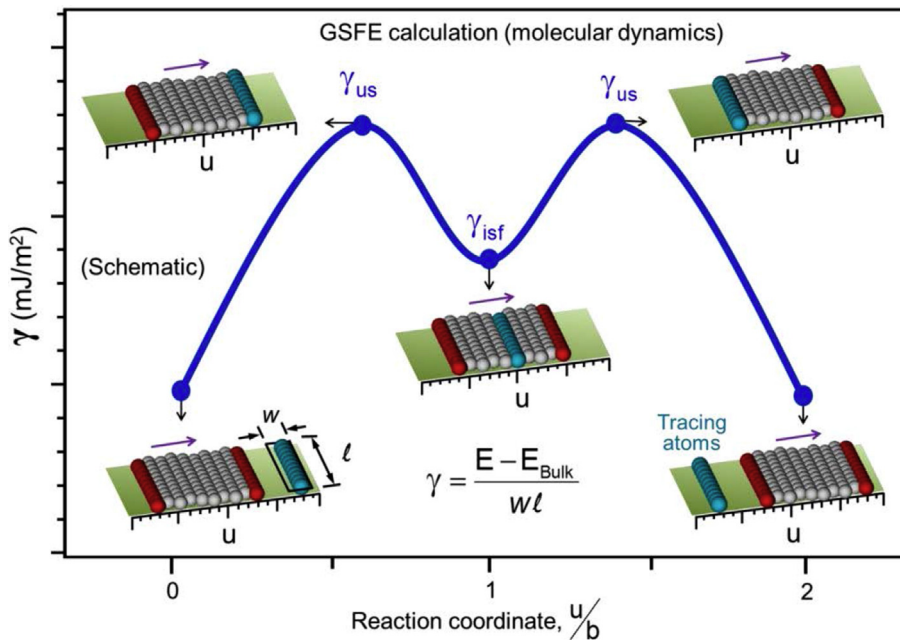## Appendix B. γ surface from molecular dynamics

Fig. B1. GSFE curve calculated during the actual glide of an extended dislocation in molecular dynamics.

Fig. B1 illustrates the procedure to calculate the γ surface in molecular dynamics simulations during the glide of a dislocation. A row of "tracing atoms" are selected for constantly monitoring the differential between bulk and slip-influenced potential energy, $\Delta E = E - E_{bulk}$. The dimensions of the tracing atomic area (w times l) are chosen carefully to ensure convergence of the calculated fault energy levels (which occurs at larger l and smaller w values (Chowdhury et al., 2013)). The fault energy γ equals to the ratio, $\frac{\Delta E}{wl}$ (Vitek, 1968). The insets in Fig. B1 show the location of the extended dislocation with respect to the tracing atoms, and the corresponding γ levels. This method can be used in computing the γ_{us} near a local stress concentration (e.g. a twin boundary, residual dislocation etc.).

References

Abuzaid, W.Z., Sangid, M.D., Carroll, J.D., Sehitoglu, H., Lambros, J., 2012. Slip transfer and plastic strain accumulation across grain boundaries in Hastelloy X. J. Mech. Phys. Solids 60, 1201–1220.

Apostol, F., Mishin, Y., 2011. Hydrogen effect on shearing and cleavage of Al: a first-principles study. Phys. Rev. B 84, 104103.

Asaro, R.J., Kulkarni, Y., 2008. Are rate sensitivity and strength effected by cross-slip in nano-twinned fcc metals. Scr. Mater. 58, 389–392.

Asaro, R.J., Suresh, S., 2005. Mechanistic models for the activation volume and rate sensitivity in metals with nanocrystalline grains and nano-scale twins. Acta Mater. 53, 3369–3382.

Austin, R.A., McDowell, D.L., 2011. A dislocation-based constitutive model for viscoplastic deformation of fcc metals at very high strain rates. Int. J. Plast. 27, 1–24.

Bailey, J., Hirsch, P., 1960. The dislocation distribution, flow stress, and stored energy in cold-worked polycrystalline silver. Philos. Mag. 5, 485–497.

Baker, S.P., 2001. Plastic deformation and strength of materials in small dimensions. Mater. Sci. Eng. A 319, 16–23.

Basinski, Z., Basinski, S., 1964. Dislocation distributions in deformed copper single crystals. Philos. Mag. 9, 51–80.

Beeston, B., Dillamore, I., Smallman, R., 1968. The stacking-fault energy of some nickel-cobalt alloys. Metal Sci. 2, 12–14.

Cai, W., Bulatov, V.V., Chang, J., Li, J., Yip, S., 2004. Dislocation core effects on mobility. Dislocations Solids 12, 1–80.

Chaboche, J.-L., Gaubert, A., Kanouté, P., Longuet, A., Azzouz, F., Mazière, M., 2013. Viscoplastic constitutive equations of combustion chamber materials including cyclic hardening and dynamic strain aging. Int. J. Plast. 46, 1–22.

Chandran, M., Sondhi, S., 2011. First-principle calculation of stacking fault energies in Ni and Ni-Co alloy. J. Appl. Phys. 109, 103525.

Cheng, B., Ngan, A.H., 2013. The crystal structures of sintered copper nanoparticles: a molecular dynamics study. Int. J. Plast. 47, 65–79.

Chowdhury, P., Sehitoglu, H., Abuzaid, W., Maier, H., 2015. Mechanical response of low stacking fault energy Co–Ni alloys–Continuum, mesoscopic and atomic level treatments. Int. J. Plast. 71, 32–61.

Chowdhury, P.B., 2011. Fatigue Crack Growth (FCG) Modeling in the Presence of Nano-obstacles. University of Illinois at Urbana-Champaign.

Chowdhury, P.B., Sehitoglu, H., Rateick, R.G., 2014a. Predicting fatigue resistance of nano-twinned materials: part I–role of cyclic slip irreversibility and Peierls stress. Int. J. Fatigue 68, 277–291.

Chowdhury, P.B., Sehitoglu, H., Rateick, R.G., 2014b. Predicting fatigue resistance of nano-twinned materials: part II–Effective threshold stress intensity factor range. Int. J. Fatigue 68, 292–301.

Chowdhury, P.B., Sehitoglu, H., Rateick, R.G., Maier, H.J., 2013. Modeling fatigue crack growth resistance of nanocrystalline alloys. Acta Mater. 61, 2531–2547.

Collins, D., Stone, H., 2014. A modelling approach to yield strength optimisation in a nickel-base superalloy. Int. J. Plast. 54, 96–112.

Deng, C., Sansoz, F., 2009a. Fundamental differences in the plasticity of periodically twinned nanowires in Au, Ag, Al, Cu, Pb and Ni. Acta Mater. 57, 6090–6101.

Deng, C., Sansoz, F., 2009b. Size-dependent yield stress in twinned gold nanowires mediated by site-specific surface dislocation emission. Appl. Phys. Lett. 95, 091914.

Dreizler, R.M., Engel, E., 2011. Density Functional Theory. Springer.

Estrin, Y., Mecking, H., 1984. A unified phenomenological description of work hardening and creep based on one-parameter models. Acta Metall. 32, 57–70.

Evans, J., 1974. Heterogeneous shear of a twin boundary in α-brass. Scr. Metall. 8, 1099–1103.

Ezaz, T., Sangid, M.D., Sehitoglu, H., 2011. Energy barriers associated with slip–twin interactions. Philos. Mag. 91, 1464–1488.

Gallagher, P., 1970. The influence of alloying, temperature, and related effects on the stacking fault energy. Metall. Trans. 1, 2429–2461.

Gleiter, H., 2000. Nanostructured materials: basic concepts and microstructure. Acta Mater. 48, 1–29.

Gu, R., Ngan, A., 2013. Dislocation arrangement in small crystal volumes determines power-law size dependence of yield strength. J. Mech. Phys. Solids 61, 1531–1542.

Hall, E., 1951. The deformation and ageing of mild steel: III discussion of results. Proc. Phys. Soc. Sect. B 64, 747.

Hartley, C.S., Blachon, D.L., 1978. Reactions of slip dislocations at coherent twin boundaries in face-centered-cubic metals. J. Appl. Phys. 49, 4788–4796.

Hirth, J.P., Lothe, J., 1982. Theory of Dislocations.

Howie, A., Swann, P., 1961. Direct measurements of stacking-fault energies from observations of dislocation nodes. Philos. Mag. 6, 1215–1226.

Humphrey, W., Dalke, A., Schulten, K., 1996. VMD: visual molecular dynamics. J. Mol. Graph. 14, 33–38.

Jackson, P., Basinski, Z., 1967. Latent hardening and the flow stress in copper single crystals. Can. J. Phys. 45, 707–735.

Jin, Z.-H., Gumbsch, P., Albe, K., Ma, E., Lu, K., Gleiter, H., Hahn, H., 2008. Interactions between non-screw lattice dislocations and coherent twin boundaries in face-centered cubic metals. Acta Mater. 56, 1126–1135.

Jin, Z.-H., Gumbsch, P., Ma, E., Albe, K., Lu, K., Hahn, H., Gleiter, H., 2006. The interaction mechanism of screw dislocations with coherent twin boundaries in different face-centred cubic metals. Scr. Mater. 54, 1163–1168.

Joos, B., Ren, Q., Duesbery, M., 1994. Peierls-Nabarro model of dislocations in silicon with generalized stacking-fault restoring forces. Phys. Rev. B 50, 5890.

Kacher, J., Eftink, B., Cui, B., Robertson, I., 2014. Dislocation interactions with grain boundaries. Curr. Opin. Solid State Mater. Sci. 18, 227–243.

Karnthaler, H., 1978. The study of glide on {001} planes in fcc metals deformed at room temperature. Philos. Mag. A 38, 141–156.

Koizumi, Y., Nukaya, T., Suzuki, S., Kurosu, S., Li, Y., Matsumoto, H., Sato, K., Tanaka, Y., Chiba, A., 2012. Suzuki segregation in Co–Ni-based superalloy at 973K: an experimental and computational study by phase-field simulation. Acta Mater. 60, 2901–2915.

Kresse, G., Furthmüller, J., 1996. Efficiency of ab-initio total energy calculations for metals and semiconductors using a plane-wave basis set. Comput. Mater. Sci. 6, 15–50.

Kumar, K., Van Swygenhoven, H., Suresh, S., 2003. Mechanical behavior of nanocrystalline metals and alloys. Acta Mater. 51, 5743–5774.

Lee, T., Robertson, I., Birnbaum, H., 1990. An in Situ transmission electron microscope deformation study of the slip transfer mechanisms in metals. Metall. Trans. A 21, 2437–2447.

Li, J., 2003. AtomEye: an efficient atomistic configuration viewer. Model. Simul. Mater. Sci. Eng. 11, 173.

Li, L., Ghoniem, N.M., 2009. Twin-size effects on the deformation of nanotwinned copper. Phys. Rev. B 79, 075444.

Li, X., Wei, Y., Lu, L., Lu, K., Gao, H., 2010. Dislocation nucleation governed softening and maximum strength in nano-twinned metals. Nature 464, 877–880.

Lu, G., 2005. The Peierls–Nabarro Model of Dislocations: a Venerable Theory and its Current Development. In: Handbook of Materials Modeling. Springer, pp. 793–811.

Lu, L., Chen, X., Huang, X., Lu, K., 2009a. Revealing the maximum strength in nanotwinned copper. Science 323, 607–610.

Lu, L., Dao, M., Zhu, T., Li, J., 2009b. Size dependence of rate-controlling deformation mechanisms in nanotwinned copper. Scr. Mater. 60, 1062–1066.

Lu, L., Shen, Y., Chen, X., Qian, L., Lu, K., 2004. Ultrahigh strength and high electrical conductivity in copper. Science 304, 422–426.

Mahajan, S., Chin, G., 1973. Twin-slip, twin-twin and slip-twin interactions in Co-8 wt.% Fe alloy single crystals. Acta Metall. 21, 173–179.

McDowell, D.L., 2010. A perspective on trends in multiscale plasticity. Int. J. Plast. 26, 1280–1309.

Meyers, M.A., Mishra, A., Benson, D.J., 2006. Mechanical properties of nanocrystalline materials. Prog. Mater. Sci. 51, 427–556.

Miller, B., Fenske, J., Su, D., Li, C.-M., Dougherty, L., Robertson, I.M., 2006. Grain boundary responses to local and applied stress: an in situ TEM deformation study. In: MRS Proceedings. Cambridge Univ Press, pp. 0976-EE0902-0901.

Müllner, P., Solenthaler, C., 1997. On the effect of deformation twinning on defect densities. Mater. Sci. Eng. A 230, 107–115.

Nabarro, F., 1947. Dislocations in a simple cubic lattice. Proc. Phys. Soc. 59, 256.

Narutani, T., Takamura, J., 1991. Grain-size strengthening in terms of dislocation density measured by resistivity. Acta Metall. Mater. 39, 2037–2049.

Ngan, A., 1995. A critique on some of the concepts regarding planar faults in crystals. Philos. Mag. Lett. 72, 11–19.

Ogata, S., Li, J., Yip, S., 2002. Ideal pure shear strength of aluminum and copper. Science 298, 807–811.

Peierls, R., 1940. The size of a dislocation. Proc. Phys. Soc. 52, 34.

Petch, N., 1953. The cleavage strength of polycrystals. J. Iron Steel Inst. 174, 25–28.

Plimpton, S., 1995. Fast parallel algorithms for short-range molecular dynamics. J. Comput. Phys. 117, 1–19.

Pun, G.P., Mishin, Y., 2012. Embedded-atom potential for hcp and fcc cobalt. Phys. Rev. B 86, 134116.

Rice, J.R., 1971. Inelastic constitutive relations for solids: an internal-variable theory and its application to metal plasticity. J. Mech. Phys. Solids 19, 433–455.

Rice, J.R., 1992. Dislocation nucleation from a crack tip: an analysis based on the Peierls concept. J. Mech. Phys. Solids 40, 239–271.

Sangid, M.D., Ezaz, T., Sehitoglu, H., 2012. Energetics of residual dislocations associated with slip–twin and slip–GBs interactions. Mater. Sci. Eng. A 542, 21–30.

Sangid, M.D., Pataky, G.J., Sehitoglu, H., Rateick, R.G., Niendorf, T., Maier, H.J., 2011. Superior fatigue crack growth resistance, irreversibility, and fatigue crack growth–microstructure relationship of nanocrystalline alloys. Acta Mater. 59, 7340–7355.

Schoeck, G., 1994. The generalized Peierls–Nabarro model. Philos. Mag. A 69, 1085–1095.

Schoeck, G., 2005. The Peierls model: progress and limitations. Mater. Sci. Eng. A 400, 7–17.

Seeger, A., Diehl, J., Mader, S., Rebstock, H., 1957. Work-hardening and work-softening of face-centred cubic metal crystals. Philos. Mag. 2, 323–350.

Suzuki, H., 1962. Segregation of solute atoms to stacking faults. J. Phys. Soc. Jpn. 17, 322–325.

Tadmor, E.B., Miller, R.E., 2011. Modeling Materials: Continuum, Atomistic and Multiscale Techniques. Cambridge University Press.

Valiev, R., 2004. Nanostructuring of metals by severe plastic deformation for advanced properties. Nat. Mater. 3, 511–516.

Vitek, V., 1968. Intrinsic stacking faults in body-centred cubic crystals. Philos. Mag. 18, 773–786.

Wang, J., Huang, H., 2006. Novel deformation mechanism of twinned nanowires. Appl. Phys. Lett. 88, 203112.

Witkin, D., Lavernia, E.J., 2006. Synthesis and mechanical behavior of nanostructured materials via cryomilling. Prog. Mater. Sci. 51, 1–60.

Wu, Z., Zhang, Y., Srolovitz, D., 2009. Dislocation–twin interaction mechanisms for ultrahigh strength and ductility in nanotwinned metals. Acta Mater. 57, 4508–4518.

Zhang, X., Deng, H., Xiao, S., Li, X., Hu, W., 2013. Atomistic simulations of solid solution strengthening in Ni-based superalloy. Comput. Mater. Sci. 68, 132–137.

Zhou, X., Johnson, R., Wadley, H., 2004. Misfit-energy-increasing dislocations in vapor-deposited CoFe/NiFe multilayers. Phys. Rev. B 69, 144113.

Zhu, L., Qu, S., Guo, X., Lu, J., 2015. Analysis of the twin spacing and grain size effects on mechanical properties in hierarchically nanotwinned face-centered cubic metals based on a mechanism-based plasticity model. J. Mech. Phys. Solids 76, 162–179.

Zhu, L., Ruan, H., Li, X., Dao, M., Gao, H., Lu, J., 2011a. Modeling grain size dependent optimal twin spacing for achieving ultimate high strength and related high ductility in nanotwinned metals. Acta Mater. 59, 5544–5557.

Zhu, T., Gao, H., 2012. Plastic deformation mechanism in nanotwinned metals: an insight from molecular dynamics and mechanistic modeling. Scr. Mater. 66, 843–848.

Zhu, T., Li, J., Samanta, A., Kim, H.G., Suresh, S., 2007. Interfacial plasticity governs strain rate sensitivity and ductility in nanostructured metals. Proc. Natl. Acad. Sci. 104, 3031–3036.

Zhu, Y., Wu, X., Liao, X., Narayan, J., Kecskes, L., Mathaudhu, S., 2011b. Dislocation–twin interactions in nanocrystalline fcc metals. Acta Mater. 59, 812–821.